AN ABSTRACT OF THE THESIS OF

Saangrut Sangplung for the degree of Doctor of Philosophy in Mechanical Engineering presented on September 7, 2007.

Title: Numerical Study of Droplet Formation with Nozzle Dynamics and Multiple Droplet Impingement

Abstract approved:

James A. Liburdy

Droplet formation from a flexible nozzle plate driven by a prescribed-waveform excitation of a piezoelectric is numerically investigated using a computational fluid dynamics (CFD) model with the VOF method. The droplet generator with a flexible nozzle plate, which is free to vibrate due to the pressure acting on the plate, is modeled in a computational domain. The CFD analysis includes the fluid-structure interaction between fluid and a flexible plate using large deflection theory. The problem is characterized by the nondimensional variables based on the capillary parameters of time, velocity, and pressure. The CFD model is validated with experiment results. This study examines the characteristics of the applied waveforms and nozzle plate material properties to change the vibrational characteristics of the nozzle plate. The effect of fluid properties on the droplet formation process is also investigated focusing on surface tension and viscous forces. The mechanism of the droplet formation excited by a drop-on-demand piezoelectric waveform is investigated using a step-function and a

pulse waveform. The piezoelectric displacement plays an important role in generating either forward-driven momentum or a suction pressure inside the chamber. For the step-function waveform, the nondimensional applied impulse is defined and used to characterize the post-breakoff droplet volume. Increasing the impulse of the piezoelectric can be used to cause a faster droplet velocity and it is shown that the vibration of the nozzle plate has a strong effect on the droplet velocity, shape, and volume. Surface tension has strong influence on the droplet formation characteristics which is in contrast to a viscous force that makes little difference on the droplet formation for a range of viscosities studied. For the combination of a fluid with high surface tension and the most flexible nozzle plate, this system can cause the droplet not to be ejected from the nozzle.

Successive droplet impingement onto a solid surface is numerically investigated using a CFD multiphase flow model (VOF method). The main focus of this study is to better understand the hydrodynamics of the non-splash impingement process, particularly the effect of a dynamic contact angle and fluid properties along with the interaction between successive droplets while they are impinging onto a solid surface. The pre-impact droplet conditions are prescribed based on a spherical droplet diameter, velocity, and inter-droplet spacing. The molecular kinetic theory is used to model the dynamic contact angle as a function of a contact line velocity. The numerical scheme is validated against experiment al results. In the impact spreading and receding processes, results are analyzed to determine the nondimensional deformation characteristics of both single and successive droplet impingements with the variation of fluid properties such as surface tension and dynamic viscosity. These characteristics include spreading ratio, spreading velocity, and a dynamic contact angle. The inclusion of a dynamic

contact angle is shown to have a major effect on droplet spreading. In successive droplet impingement, the second drop causes a surge of spreading velocity and contact angle with an associate complex recirculating flow near the contact line after it initially impacts the preceding droplet when it is in an advancing condition. This interaction is less dramatic when the first drop is receding or stationary. The surface tension has the most effect on the maximum spreading radius in both single and successive droplet impingements. In contrast to this, the viscosity directly affects the damping of the spreading-receding process.

NUMERICAL STUDY OF DROPLET FORMATION WITH NOZZLE DYNAMICS AND MULTIPLE DROPLET IMPINGEMENT

by

Saangrut Sangplung

A THESIS

submitted to

Oregon State University

in partial fulfillment of

the requirements for the

degree of

Doctor of Philosophy

Presented September 7, 2007

Commencement June 2008

Doctor of Philosophy thesis of Saangrut Sangplung presented on September 7, 2007

APPROVED:

_____

Major Professor, representing Mechanical Engineering

_____

Head of the School of Mechanical Engineering, Industrial, and Manufacturing Engineering

_____

Dean of the Graduate School

I understand that my thesis will become part of the permanent collection of Oregon State University libraries. My signature below authorizes release of my thesis to any reader upon request.

_____

Saangrut Sangplung, Author

ACKNOWLEDGEMENTS

I would like to express my sincere gratitude to Dr. James A Liburdy for his guidance and support during my graduate study. I would also like to thank my graduate committee members: Dr. Solomon C. Yim, Dr. Deborah V. Pence, Dr. Vinod Narayanan, and Dr. Brain Woods (GCR), for guidance during my studies. Last, the greatest appreciation is for my parents, sister, wife and son, Kyle, for their encouragement and support during this study.

TABLE OF CONTENTS

Page

TABLE OF CONTENTS (Continued)

Page

LIST OF FIGURES

LIST OF FIGURES (Continued)

Figure Page

LIST OF FIGURES (Continued)

Figure Page

LIST OF TABLES

Table Page

NOMENCLATURE

A_1, A_2 = Overshoot and undershoot radii of the spreading droplet

C, Ci = Volume fraction, volume fraction of specie i^{th}

c_i = Mass fraction

c_l = Volume fraction

C_θ = Damping ratio of a droplet spreading-receding cycle

Ca = Capillary number, $Ca = \frac{\mu V_{cl}}{\sigma}$

E = Young modulus (GPa)

E* = Nondimensional stiffness, E/P_c

E_c = Capillary stiffness

F_i, F_{c_i} = Source term in momentum equation, Source term of specie i^{th}

h = Nozzle plate thickness

I* = Nondimensional impulse

K = Boltzmann's constant

l = Position of the leading edge

L* = Nondimensional leading edge position, l/l_c

l_c = Capillary length

m, m_i = Mass, mass of specie i^{th}

n = Number of adsorption sites per unit area

P = Pressure

P* = Nondimensional pressure, P/P_c

P_c = Capillary pressure

r = Radial distance, or Instantaneous spreading radius of droplet

R* = Spreading ratio, r/ R_0

NOMENCLATURE (continued)

R^*_{max} = Maximum Spreading radius, r_{max}/ R_0

Re = Reymolds number, $\mathrm{Re} = \frac{\rho D_0 U_0}{\mu}$

r_{max} = Maximum spreading radius of droplet

R_o = Radius of a pre-impact droplet

T = Absolute temperature

t = Time

t_c = Capillary time

t_{rampup} = Rampup period of a piezoelectric

U^* = Nondimensional droplet velocity, u/u_c

U^*_{CL} = Nondimensional contact line velocity, U_{CL} / U_0

u,v,w = Velocity components

u_c = Capillary velocity

U_{CL} = Contact line velocity

U_o = Pre-impact droplet velocity

V = Volume

V^* = Nondimensional volume, V/V_c

V_c = Capillary volume

W = Work per unit area done by surface tension force

w = Plate Displacement in equation

We = Weber number, $We = \frac{\rho D_0 U_0^2}{\sigma}$

x,y,z = Distances, rectangular coordinate

x,y,z = Distances, rectangular coordinate

NOMENCLATURE (continued)

Greek symbols

δ_{plate} = Nozzle plate displacement

δ^*_{plate} = Nondimensional plate displacement scaled by h

δ^*_{piezo} = Nondimensional piezoelectric displacement scaled by h

δ^*_{max} = Nondimensional maximum piezoelectric displacement scaled by h

κ = Radii of curvature (m)

κ_ω = Net frequency of molecular displacement (1/s)

κ^o_ω = Equilibrium frequency of molecular displacement (1/s)

λ = Length of molecular displacement

μ, μ_l = Viscosity, viscosity of heavy fluid in VOF method

μ^* = Dynamic Viscosity ratio between nominal fluid and water

ρ, ρ_i = Density, density of specie i^{th}

Θ_E = Equilibrium contact angle

Θ_D = Dynamic contact angle

σ = Surface tension (N/m)

σ^* = Ratio of fluid surface tension to water's surface tension

τ = Nondimensional time, t/t_c

τ_{rampup} = Nondimensional rampup time, t_{rampup}/t_c

φ = Airy stress function

τ = Nondimensional time, $t\ U_0 / R_0$

$\Delta\tau$ = Nondimensional inter-droplet time interval

NUMERICAL STUDY OF DROPLET FORMATION WITH NOZZLE DYNAMICS AND MULTIPLE DROPLET IMPINGEMENT

CHAPTER 1

INTRODUCTION

Droplet formation is a microfluidics application in areas such as printer heads, medical dispensers, thin film coating, etc. The effort to control either the size or velocity of the droplet after break-off is of great importance. Drop-on-demand (DOD) systems were introduced to improve the quality of droplets while providing delivery control. One DOD systems is a piezoelectric DOD system, which can eject droplets under the applied excitation of the piezoelectric plate. This study investigates the dynamic mechanisms of piezoelectric DOD droplet formation along with the possibility of improving the characteristics of droplets after break-off. The concept is to include a flexible nozzle plate on top of the fluid chamber. Droplet formation with a flexible nozzle plate was first patented by Tony Cruz-Uribe from Hewlett-Packard (HP), US Patent number 7219970. The basis of this design is the use of flextensional technology, which relates to the deflection of a thin flexible membrane and the fluid boundary. In contrast to this, Yang and Liburdy [2004] studied the effect of a passively moving boundary (a flexible nozzle plate) and its effect on different characteristics of droplet formation. In this latter case, the fluid structure interaction needs to be taken into account.

Droplet impingement onto a solid surface is an important field of current research in heat transfer, inkjet printing, coating, etc. The major objective of droplet impingement works is usually to determine the characteristics of spreading and receding processes of droplet impingement on the solid surface. Most applications are governed by surface tension and the interactions between liquid–solid interfaces. The characteristics of the flow and the change of the contact angle near the contact line are important in studying droplet impingement. This contact angle has a direct effect to both spreading and receding processes. Dynamic contact angle model has been well defined in the past years in which most of them are based on the empirical data and defined as function of contact line velocity. The contact angle has directly effect to the surface tension force at the contact line and consequently affects the spreading and receding of the droplet. Moreover, the successive droplet impingement is also the other major part in this thesis after the contact angle is well defined by using the validated model.

The great motivation of this research is to study the behavior of multiphase flow under the influence of surface tension such as droplet formation and droplet impingement. The numerical method and the high-end technology of the latest computers and software are the tools that allow these complicated problems to be overcome. This computational study using numerical software is conducted to predict the characteristics of the flow; this research is mainly concerned with the free-surface flow with a focus on the droplet formation and droplet impact.

The main objectives of the droplet formation in this study are to investigate the droplet formation under the effects of following parameters: flexibility of a nozzle plate, applied waveforms, and fluid properties (surface tension and viscosity). In this work, the geometries of a droplet generator, a piezoelectric plate and a nozzle

plate are modeled in a computational domain. Two types of piezoelectric waveforms are applied to the bottom plate as an impulse input to eject droplet out of the orifice hole. These two waveforms are defined as a piezoelectric displacement as a function of time. The step-function input is first employed to obtain the droplet formation causing by the forward driving momentum without any suction pressure from the movement of the piezoelectric plate. For this step-function input, the piezoelectric is held at its maximum displacement for all time after it reaches this maximum point. The other type of waveform is a pulse-function where the piezoelectric is pulled back to the origin after reaching the maximum displacement for a certain time. During the fall of the piezoelectric waveform during the formation process, suction pressure is generated and causes a negative force from inside of fluid chamber which then pulls on the thread of the liquid jet. This phenomenon can cause different characteristics of droplet formation such as changes to the droplet volume and break-off time.

For the study of the effect of nozzle plate flexibility on the droplet formation, the geometric parameters of a nozzle plate, diameter and thickness, are fixed. The varied variable is the stiffness of the nozzle plate. The variation of fluid properties is also included as part of the droplet study. In this section, two major fluid properties, surface tension and dynamic viscosity are varied to identify the effects on droplet formation. The results of this study are represented in nondimensional form using scales defined by the capillary pressure, capillary time and capillary length. The characteristics of droplet formation are reported as follows: droplet volume, post-break-off droplet velocity, and break-off time.

The objective of the droplet impact study is to understand the hydrodynamics of the impingement process with contact angle dynamics, particularly the

interactions between successive droplets while they are impinging onto a solid surface. The effects of several key parameters on the hydrodynamics of the collision are studied. These include: equilibrium contact angle, fluid properties, and the relative phase of successive droplet impingement. In simulating droplet impingement, the solid wall is created in the computational domain and it is assumed that a single spherical liquid droplet of diameter D_0 with constant surface tension impinges on a flat rigid stationary surface with velocity U_0. This numerical model neglects the interaction between the droplet and air, and focus on the interface tension between the droplets and target surface while allowing for a variation of the dynamic contact angle. An appropriate dynamic contact angle model is determined and validated with experimental results.

The first effect to be studied in droplet impingement is the equilibrium contact angle. This equilibrium contact angle normally indicates the wettability between droplet impingement and a solid surface. At an equilibrium contact angle higher than 90 degree, the process is considered as a nonwettable one. Next, in successive droplet impingement, a simple superposition of two single droplets is used as an initial condition. The initial inter-droplet spacing is used to define the phase of successive droplet impingement. The initial conditions of the second droplet such as the velocity and size are identical to the first droplet. The variation of fluid properties is also investigated in this work with the exact conditions for both single and successive droplet impingements. There are only two fluid properties considered of interest, which are surface tension and dynamic viscosity. The characteristics of droplet impingement are reported as follows: spreading rate, maximum spreading radius, contact angle, and contact line velocity versus time. Also included are a series of velocity vector field plots for both single and

successive droplet impingement used to explain the details associated with successive droplet impingement.

The thesis is organized as follows. Chapter 2 presents a literature review for pertinent topics. The mathematical model of fluid flow model, nonlinear large deflection plate equations and molecular kinetic theory models are described in Chapter 3. The numerical methods used to solve the problem and the geometry of the computational domains is given in Chapter 4. Chapter 5 provides the validation of the numerical solutions with experimental results and the results of simulations for both droplet formation and successive droplet impingement. Chapter 6 contains the conclusion of this research including suggestions for future research related to this topic.

CHAPTER 2

LITERATURE REVIEW

The study of hydrodynamics and instability of the free surface flow such droplet formation and impingement started in late nineteenth century by the famous scientists such as Lord Rayleigh and Worthington. In this thesis, the understanding of the physics of the droplet formation and impingement was sought first, so most of physics perspectives from the previous literatures are presented in this section. The droplet formation and its mechanism are first discussed as follows: droplet-on-demand droplet formation, fluid-structure-interaction, and numerical solutions for both free surface flow and droplet formation. For the droplet impingement, the previous experimental and numerical results are reviewed. The other key concept in this work is to understand the impinging conditions: splash and non-splash. Moreover, the dynamics of contact angles along the spreading and receding process is one of major ideas to be comprehended.

2.1 DROPLET FORMATION

The phenomenon of droplet formation in a liquid jet has been studied by many authors. The earliest analysis appears to be that of Rayleigh [1892], who made a linearized stability analysis of a nonviscous liquid jet. His mathematical model was developed to meet the phenomena of uniform drop formation from a stream of liquid ejecting from an orifice based on a linearized stability analysis of a nonviscous liquid jet. Weber [1931] used a similar approach as Rayleigh, but produced a much more useful result by making several simplifying assumptions. The linearization makes closed-form solutions possible including solutions for stability of the stream and for drop breakup time under a given initial perturbation and external excitation.

The formulations of the Navier-Stokes equations for incompressible flow with a free surface became a useful model employed in a number of studies in an effort to understand the physical mechanisms governing droplet formation. The drop-on-demand (DOD) study was initiated by Beasley [1977] with the model for the fluid ejection driven by an impulse jet. A few years later, Kyser [1981] designed the cavity containing the fluid for the Impulse Ink Jet. In the 1980's, Fromm [1984] obtained the numerical solutions for DOD jets based on a 2D mathematical model. Sheild et al. [1987] compared a simplified 1D numerical simulation with experiment results. Also, for 1D numerical model of droplet, Adams and Roy [1986] present the Macormack's predictor-corrector algorithm to solve one-dimensional model equations of drop development from a drop-on-demand inkjet. In recent years, Drop-on-Demand (DoD) has been in a focus of fluid mechanist.

The droplet breakup from a liquid jet of Newtonian fluid has been deeply investigated by several researchers based on a 1D jet approximation. Such models predicts the breakup of jets in finite time, described by a similarity solution by Eggers [1995]. On the other hand, it is well-known that viscoelasticity and other non-Newtonian effects slow down the breakup process by reducing the effect of surface tension as shown by Renardy [1994, 1995] and Yarin [1993]. However, pinch-off may still occur due to the surface tension force, which becomes dominant when the radius of the liquid jet is small. The droplet pinch-off process is a complex physical phenomenon where the traditional use of surface tension forces is not well understood. Egger [1993] investigated the break-off process by focusing on the singularity of a set of universal exponential forms of the solution of the Navier-Stokes equations. Moreover, the thread breakup was also studied by Henderson et al. [1997] and Brenner et al. [1997]. In recent CFD simulation using

the finite volume method, Fawehinmi et al. [2005] defined the break-off process by the scale of volume fraction corresponding to the mesh size in a computational domain.

A method developed to track free surfaces is the Volume of Fluid (VOF) method introduced by C.W. Hirt [1981]. The VOF model has become a popular method in free surface models used in CFD computational programs. For this method, the volume fraction between light and heavy fluid is used to define the region occupied by fluid. An additional method used with VOF for modeling surface tension effects on fluid motion is the continuum surface force model developed by Brackbill et al. [1992]. This method is employed to determine the surface tension force between two immiscible fluids by the volume fraction at the interface.

In this study, fluid structure interactions are important in determining the interplay of fluid internal pressure and nozzle plate deflection which then affects droplet formation. Considerable efforts have been made to develop models for the simulation of microfluidic devices by Yarin [1993], Bourounia and Grandchamp [1996], and Krevet and Kaboth [1998]. These methods are very complex and time consuming especially if coupled analyses are performed. Only a few studies model microfluidic devices with actuation mechanisms while considering the full fluid structure interaction by Percin et al. [1998], Wijshof [1998], and Hermann and Joachim [2004].

In the nonlinear plate model, the large deflection plate equation is the model used to determine the response of plates when they are subjected to large scale force amplitudes. This massive force produces large deflection of the plate comparing to the thickness. Based on this nonlinear effect, the fundamental for

exact theory have been derived by Von Karman [1910]. The solutions of the large deflection plate equation can be determined by both analytical methods and numerical methods. There are in the literature some interesting numerical investigations, such as the one by Vogel and Skinner [1965], who studied nine combinations of boundary conditions; they considered simply supported, clamped and free edges at the inner and outer boundaries. Data references were also given in Leissa [1969] for various types of nonlinear plate geometries.

Annular and perforated plates are often in contact with a fluid on one or both sides. It is well known that natural frequencies of a thin-walled structure are strongly affected by the presence of a heavy fluid. Kubota and Suzuki [1984] presented annular plates vibrating in an annular cylindrical cavity filled with a fluid were theoretically and experimentally studied. In the paper by Amabili and Frosali [1994], the free vibrations of annular plates placed on a free surface were theoretically investigated.

2.2 DROPLET IMPINGEMENT

The drop impingement problem was first studied by Worthington [1876]. The focus of most subsequent studies has been the prediction of several features such as the maximum impact pressure by Engel [1955], the resultant flow dynamics (splash, deposition, etc.), see Hartley and Brunskill [1958], Ford and Furmidge [1967], Stow and Hadfield [1981] and Rioboo [2002]. Also, Liu et al. [2005] investigated the effect of roughness on droplet impingement. In related studies Blake and Haynes [1969] examined the kinetics of liquid/liquid displacement during spreading, and Bradley and Stow [1978] investigated the collision of liquid drops. These studies discussed precursor liquid impingement and successive droplet impact. Recently, the impact of successive droplets on a substrate was

modeled as a superposition of two single droplets impacting successively on a substrate. Tong et al. [2004] generated a numerical model for successive droplets, with a second droplet impinging on a static droplet and compared results with experimental data.

The interaction between the droplet and solid surface can be classified into conditions: splash and non-splash. For non-splash impinging condition, the momentum from an impingement is not sufficient to break up the main droplet into satellite droplets during the impact. Later, the spreading force from this momentum is dissipated along the spreading. For this reason, the droplet is able to spread and recede on the solid surface. Also, the non-splash condition is more likely to be able to be predicted and defined with some close form model for the spreading and receding. On the other hand, splashing occurs when a single droplet hits the surface and generates satellite droplets. Stow and Hadfield [1981] came up with a correlation of Reynolds and Weber numbers for the splashing threshold which is also depended on the surface roughness. Zhang and Basaran [1997] also defined the different splash correlations, but still a function of Reynolds and Weber numbers. These nondimensional variables measure the relative scale of inertial to surface tension force and viscous force to determine the condition of impingement.

The first computational analysis of droplet impingement was introduced by Harlow and Shannon [1991] by using marker and cell (MAC) method, but this work can only determine the advancing stage of droplet impingement. It can not simulate the receding of the droplet when the rebounding force is generated from the surface tension force. Madejski [1976] also defined the analytical solution of the characteristics of droplet impingement such as a maximum radius and spreading ratio as function of time. Fukai et al. [1993] used the finite element

method to simulate droplet impingement by taking gravity, viscosity, surface tension, and inertia into account, but was simplified by using a constant contact angle. Trapaga and Szekely [1986] first used a Volume of Fluid method (VOF) to investigate the spreading of droplet impingement. Their study shows the capability to simulate droplet deformation and breakup during impingement, but there are some physical discrepancies about the shape of the interface between two immiscible fluids. In recent year, the techniques of VOF method have been improved and have corrected many of its flaws. According to the latest scheme and algorithm of VOF method, Vadillo [2004] did both single and multiple droplet impact simulation and compared the results with experimental data, but this work only assumed the constant contact angle along the spreading/receding processes. The collision dynamics of successive droplet impingement was performed by Minamikawa et al. [2007].

The dynamic contact angle model is an essential feature in the study of droplet impingement, since it is important in the spreading rate, spreading velocity, and transport properties. Hoffman's model [1975] was first developed to represent a universal model for dynamic contact angle as a function of contact line velocity. Roisman et al. [2002] used Hoffman's model to investigate spreading and receding behavior of normal drop impact. Sikalo et al. [2005] employed Hoffman's function with a finite volume numerical code to predict the dynamic contact angle of the inner region and then applied this angle to the computational domain to determine the apparent contact angle. Another model of the dynamic contact angle was defined by Blake [1993] based on molecular kinetic theory. The model parameters include frequency and length of molecular displacement, which are determined by empirical relationships between contact angle and contact line velocity. Xu et al.

[2004] employed molecular motion to study a droplet spreading on a precursor film. Bayer and Megaridis [2006] provided a measure of validation of the molecular-kinetic theory with experimental results.

CHAPTER 3

MATHEMATICAL MODEL

The study of droplet formation from a flexible nozzle or orifice plate takes the interaction between the fluid and solid into account. Consequently, the nonlinear large deflection plate equation is defined and added into the numerical solver. For droplet impingement, the molecular kinetic theory model is used as a dynamics contact angle model. This model is defined as a function of contact line velocity and its parameters are based on empirical data of the specific solid surface and fluid properties such as surface tension and viscosity.

3.1 NAVIER-STOKES EQUATIONS

The mathematical model used in modeling fluid flow is the three-dimensional continuity equation and Navier-Stokes equations as follows:

$$\frac{\partial \rho}{\partial t} + \frac{\partial (\rho u_i)}{\partial x_i} = 0 \qquad (1)$$

$$\frac{D(\rho u_i)}{Dt} = -\partial_i p + \rho g_i + \mu \partial_j \partial_j u_i + F_i \qquad (2)$$

where u_i is the velocity vector with components of u, υ and w, p is the fluid pressure.

From Equation (2), the surface tension force can be considered as a source term where the external force, F_i, arbitrarily is applied to the fluid in the momentum equations. For a free surface flow, this force occurs at the interfaces of two immiscible fluids or liquid, gas and wall. The boundary condition is defined as a stress boundary where the tangential stress is assumed equal to zero and normal stress is determined by the product of the radii of curvature and surface tension. Thus, the stress boundary reduces to Laplace's formula as shown in Equation (3):

$$\Delta P = p_{liquid} - p_{gas} = \sigma\kappa \tag{3}$$

where ΔP is the surface pressure at the interface, σ is the surface tension coefficient and κ the mean surface curvature. The mean surface curvature is mathematically given by

$$\kappa = -\left(\nabla \cdot \hat{n}\right) = \frac{1}{|n|}\left[\left(\frac{n}{|n|}\cdot\nabla\right)|n| - \left(\nabla \cdot n\right)\right] \tag{4}$$

where n is a normal vector of the free surface, and the unit normal $\hat{n}$ is given by,

$$\hat{n} = \frac{n}{|n|} \tag{5}$$

For droplet impingement, the interaction between liquid, gas and solid is taken into account during droplet impingement. At the solid wall, the no-slip condition is assumed where the velocity components at the wall are equal to zero. However, the contact line is allowed to move due to the surface tension force and fluid internal pressure. The contact angle at a liquid-solid contact line needs to incorporate the contact angle in this boundary condition in which this angle would strongly affect the normal stress at the interface. The unit normal of the free surface, $\hat{n}$, at the wall contact can be determined as follow:

$$\hat{n} = \hat{n}_W \cos\theta_D + \hat{t}_W \sin\theta_D$$

where θ_D is a contact angle, $\hat{n}_W$ is the unit normal directed into the wall, and $\hat{t}_W$ is the tangent to the wall

3.2 LARGE DEFLECTION PLATE EQUATION

In this work, the nonlinear large deflection plate equation is used in the fluid flow numerical domain. The main reason is to have the plate solution match the physical plate condition as much as possible. In general, a small deflection plate is a linear model that is limited to low pressure distribution on the plate and the small

deflection of plate responses. Here are several assumptions used for the large deflection plate equation in which is not valid for the linear small deflection plate model:

- The deflection of the plate mid-surface is relatively high in comparison with the plate thickness.
- The component of stress normal to the mid-surface is significant.
- There are mid-surface straining, stretching, and contracting that occur as a result of bending.

During droplet formation, the flexible nozzle plate is considered to be one of the boundary conditions. The governing equation used to determine the boundary deflection is based on the dynamics of nonlinear large deflection plate theory from Rao [19991] as:

$$\nabla^4 \phi = -\frac{Eh}{r} w_r w_{rr}$$

$$-\frac{D}{\rho h}\nabla^4 w - \frac{c_{damping}}{\rho h}\dot{w} + \frac{1}{\rho h \cdot r}\left(\phi_r w_r\right)_r + \frac{P}{\rho h} = \ddot{w} \qquad (6)$$

where φ is airy stress function, w is the plate displacement, $\dot{w}$ is the plate velocity, $\ddot{w}$ is the plate acceleration, P is the pressure acting on the nozzle plate, D is the flexural rigidity, and $c_{damping}$ is a damping ratio.

From Equation (6), the nonlinear plate model is added to the numerical domain subjected to two types of boundary conditions: free edge and clamped edge along with a prescribed pressure distribution. These two boundary conditions are the constraints at the inner and outer edge of the plate respectively. These conditions can be considered as an annular plate as shown in Figure 3.1.

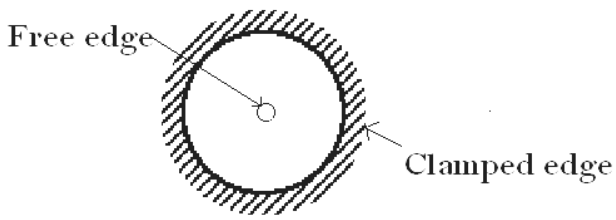

Fig. 3.1. Annular clamped plate

At the clamped edge, the definition for this clamped edge boundary condition can be expressed by

$$w = 0 \qquad u = 0$$

$$\frac{\partial w}{\partial r} = 0 \qquad \varepsilon_r = 0 \qquad \varepsilon_\theta = 0$$

where ε_r and ε_θ are the strain in radial and angular axis.

For the inner edge of the plate, a free edge is assumed, so the differential terms for symmetrical bending can be derived with the conditions of $M_r = 0$ (radial moment) and $V_r = Q_r = 0$ (radial shear force and shear stress). The resulting expressions are given as follows:

$$M_r = 0; \quad -D\left(\frac{\partial^2 w}{\partial r^2} + \frac{v}{r}\frac{\partial w}{\partial r}\right) = 0 \tag{7}$$

$$Q_r = 0; \quad -D\left(\frac{\partial^3 w}{\partial r^3} + \frac{1}{r}\frac{\partial^2 w}{\partial r^2} - \frac{1}{r^2}\frac{\partial w}{\partial r}\right) = 0 \tag{8}$$

The other major boundary condition on the plate is the pressure distribution boundary which is determined by the fluid interaction inside the chamber as shown in Figure 3.2.

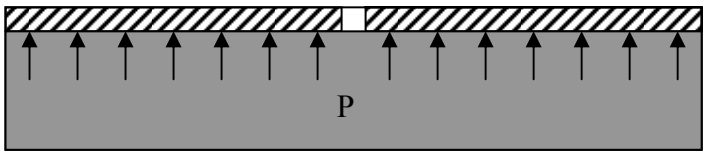

Fig. 3.2. Schematic of the pressure boundary of the plate model in the chamber.

Considered is a distributed lateral load shown in Figure 3.2, which is from the fluid pressure acting on the plate surface. This pressure *P*, presented in Figure 3.2, is the excitation of the plate model and is the pressure *P* in Equation (6). This load causes the plate to bulge out by the bending moment and shearing stress directly applied from the fluid pressure at the wall boundary. This deflection changes the shape of wall boundary and consequently the pressure distribution in the fluid, so the interaction between fluid and plate inside the chamber is important and is taken into account.

3.3 DYNAMIC CONTACT ANGLE MODELS

The most important physics for the droplet impingement is the dynamics of the contact angle. There are many dynamic contact angle models developed in the past years. Most of them are defined as functions of the contact line velocity. This correlation between contact line velocity and the contact angle are based on empirical data.

The model used to track the dynamic contact angle in this work is the molecular kinetic (M-K) theory. It was first developed by Blake [1993] based on Eyring's [1969] molecular kinetics theory. This theory assumes that the contact line velocity is depended on the contact angle in terms of the rate constant of the molecular displacement process at the solid surface. At equilibrium, the contact line is stationary, but not at the molecular level. However, the net rate of displacement is equal to zero because of the balance of both forward and backward direction of molecular displacement as follow:

$$\kappa_w^+ = \kappa_w^- = \kappa_w^0$$

where κ_w^+ is the frequency of molecular forward movement, κ_w^- is the frequency of molecular backward movement, κ_w^0 is the frequency of molecular movement at equilibrium, and subscription *w* present the wetting process.

From the Eyring's theory of reaction rate, the molecular displacement frequency can be related to the molar free energy, ΔG^*_w:

$$\kappa_w^0 = \left(\frac{kT}{h}\right)\exp\left(\frac{-\Delta G_w^*}{NkT}\right) \tag{9}$$

where k is Boltzman's constant, T is temperature, h is Plank's constant, and N is number of molecules in an energy state.

For the advancing contact line, the frequency of molecular forward displacement is greater than the backward displacement. This results in the change of shear stress at the contact line in both directions for the molecular displacement. The higher the contact line velocity, the higher the net rate of displacement and the more shear stress. The work done by shear stress per unit molecular displacement is *W* and the average work per adsorption site is *W/2n* where and *n* is the number of adsorption sites per unit area on the surface, related to the length of molecular displacement shown in Equation (11). The final expressions for both forward and backward frequencies are given by:

$$\kappa_w^+ = \left(\frac{kT}{h}\right)\exp\left(\frac{-\left(\Delta G_w^* - \frac{W}{2n}\right)}{NkT}\right)$$

$$\kappa_w^- = \left(\frac{kT}{h}\right)\exp\left(\frac{-\left(\Delta G_w^* + \frac{W}{2n}\right)}{NkT}\right)$$

and the net frequency of molecular displacement is

$$\kappa_w = \kappa_w^+ - \kappa_w^-$$

$$\kappa_w = \kappa_w^0\left(\exp\left(\frac{W}{2nkT}\right) - \exp\left(\frac{-W}{2nkT}\right)\right)$$

$$\kappa_w = 2\kappa_w^0 \sinh\left(\frac{W}{2nkT}\right) \qquad (10)$$

Next, the velocity of the contact line can be related to the characteristics of molecular displacements as follow:

$$U_{CL} = \kappa_w \lambda \qquad (11)$$

where U_{CL}, κ_w, and λ are the contact line velocity, the net frequency, and the length of molecular displacement, respectively, and *n* is related to λ by $n = 1/\lambda^2$.

From Equations (10) and (11), the velocity of the contact line is written as:

$$U_{CL} = 2\kappa_w^o \lambda \sinh\left(\frac{W}{2n\kappa T}\right) \tag{12}$$

The work per unit area of the shear stress, *W,* done by the spreading process is generated by the out-of-balance force between the surface tension of the instantaneous contact angle and the equilibrium contact angle at the contact line; *W* is expressed as

$$W = \sigma\left(\cos\theta_E - \cos\theta_D\right) \tag{13}$$

Using the dynamic contact angle, the resultant expression relating U_{CL} and θ_D is

$$U_{CL} = 2\kappa_w^o \lambda \sinh\left[\frac{\sigma}{2nkT}\left(\cos\theta_E - \cos\theta_D\right)\right] \tag{14}$$

In Equation (14), κ_w^o and λ can be determined by curve-fitting the data of the actual contact angle and its contact line velocity.

There is another promising dynamic contact angle model developed in the past years by Hoffman [1975] based on his experiments on silicone oils displacing air in glass capillaries. The dynamic contact angle based on Hoffman's Law is shown as follow:

$$\theta = f_{Hoff}\left[Ca + f_{Hoff}^{-1}(\theta_0)\right] \tag{15}$$

where θ_0 is the static contact angle, $Ca = \frac{\mu V_{cl}}{\sigma}$ is the capillary number, V_{cl} is the velocity of propagation of the contact line and $f_{Hoff}^{-1}(\cdot)$ is the inverse function of the function $f_{Hoff}(\cdot)$, which is defined as

$$f_{Hoff}(x) = \cos^{-1}\left\{1 - 2\cdot\tanh\left[5.16\cdot\left(\frac{x}{1+1.31\cdot x^{0.99}}\right)^{0.706}\right]\right\}$$

However, this model is based on Hoffman's experimental data and it is difficult to fit to other droplet impingement experimental setups.

CHAPTER 4

NUMERICAL SIMULATION

In this chapter, the methodology and numerical method are presented. The Volume of Fluid (VOF) and Continuum Surface Force (CSF) models are employed to track the free surface flow with the effect of surface tension force. Some computational criteria and algorithm of the simulations are also mentioned in detail such as pinch-off criteria, fluid structure interaction, and determination of the contact line velocity.

4.1 METHODOLOGY

The commercially available StarCD (version 3.26) and Comet (version 2.11) CFD numerical codes were used in this study using a parallel cluster (40 nodes). The finite volume method with a VOF model and a Continuum Surface Force model (CSF) was implemented.

Both droplet formation and impingement are modeled as a multi-phase flow under the influence of surface tension. The model used to track the free-surface flow is the volume of fluid (VOF) method developed by Hirt and Nichols [1981]. In this method, two types of immiscible fluids are assigned as the heavy and light fluids in which both densities, although different, are constant (incompressible flow). The existence of the heavy fluid and the interface of the two fluids are represented by a passive scalar c_l which is defined as the ratio of heavy fluid volume to the total volume in a computational cell. The relationship for c_l can be shown to be as follows:

$$\frac{\partial}{\partial t} c_l + \nabla \cdot (c_l u) = 0 \qquad (16)$$

where c_l is equal to 1 when the cell is totally occupied by heavy fluid, and $c_l = 0$ for light fluid. At the interface, c_l ranges from 0 to 1.

Volume of fluid method is not only to determine the cell that contains the interface boundary, but also defines where the fluid is located in an interface cell. The normal direction to the interface lies in the direction in which c_l changes rapidly. For this reason, the VOF method is able to track the arbitrarily oriented free surface and interface boundary with respect to the computational mesh. The advective term in Equation (16) is a key term in interface reconstruction which models the movement of the fluid through the mesh.

All physical properties are based on the passive scalar function, c_l, and the physical properties of the immiscible fluids as:

$$\begin{aligned} \rho &= \rho_g (1 - c_l) + \rho_l c_l \\ \mu &= \mu_g (1 - c_l) + \mu_l c_l \end{aligned} \tag{17}$$

This scheme is modeled by the combination of upwind and downwind schemes with a correction factor based on Courant number. This number is the ratio of fluid velocity to the grid celerity ($\Delta x/\Delta t$) over the interface angle normal to the cell face surface. The primary variables resulting from the simulation are the local time-varying velocity, pressure, and volume fraction.

The continuum surface force (CSF) model is used to determine the surface tension acting at the interface between liquid and gas phases as developed by Brackbill et al. [1992]. Surface tension at the free surface boundary is modeled with a localized volume force prescribed by CSF model. This surface tension force is an external source term, F_i in Equation (2).

Consider the effect of surface tension on a fluid interface; the surface stress boundary condition can be expressed as follow:

$$\left(p_{liq} - p_{gas} + \sigma\kappa\right)\hat{n}_i = \left(\tau_{ik}^{liq} - \tau_{ik}^{gas}\right)\hat{n}_k + \frac{\partial\sigma}{\partial x_i} \tag{18}$$

where σ is the fluid surface tension coefficient, p_{liq} and p_{gas} are the pressure in the fluid, τ is the viscous stress tensor, and $\hat{n}$ is the unit normal vector.

In this model, the surface tension is a constant and the viscous force is neglected, so the expression of the boundary condition shown in Equation (18) reduces to,

$$p_{gas} - p_{liq} = \sigma\kappa$$

where σ is the surface tension coefficient and κ the mean surface curvature. The curvature of a free surface, κ is calculated from

$$\kappa = -\left(\nabla \cdot \hat{n}\right)$$

In the combination of VOF method CSF model, the interface is replaced by volume fraction, c_l, whose normals are gradients of c_l.

$$n = \nabla c_l$$

The unit normal is thus

$$\hat{n} = \frac{n}{|n|} = \frac{\nabla c_l}{|\nabla c_l|}$$

where κ is determined by:

$$\kappa = -\nabla \cdot \left(\frac{\nabla c_l}{|\nabla c_l|}\right) \tag{19}$$

The computation of the surface tension force comes from the results from neighborhood mesh at the interface, so the effect of surface tension should be confined to the neighborhood of the interface.

4.2 SIMULATION FOR DROPLET FORMATION

Numerical Grid

A model of the droplet generator and its cross-sectional view and its computational mesh are shown in Figure 4.1 and 4.2 respectively. In the CFD solution domain, the entire chamber inside the droplet generator is modeled using a three-dimensional axisymmetric cylindrical mesh. The surrounding space outside the nozzle exit is also included in the domain to track the interaction between the two phases: liquid and gas. To validate the numerical solution, two criteria were used to check the accuracy of the CFD model: grid-dependent solution and experimental validation. In this section, the grid-independent is discussed and then the comparison with the experimental result is presented with the results.

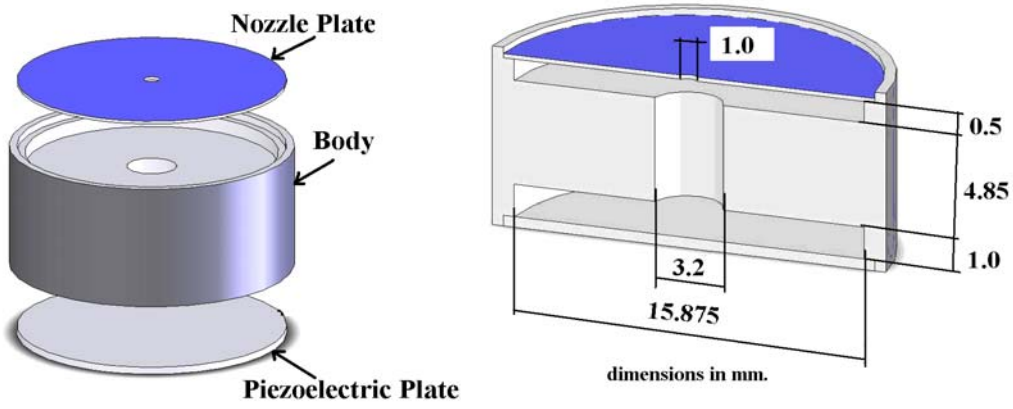

Fig. 4.1. Schematic of the droplet generator modeled in this study.

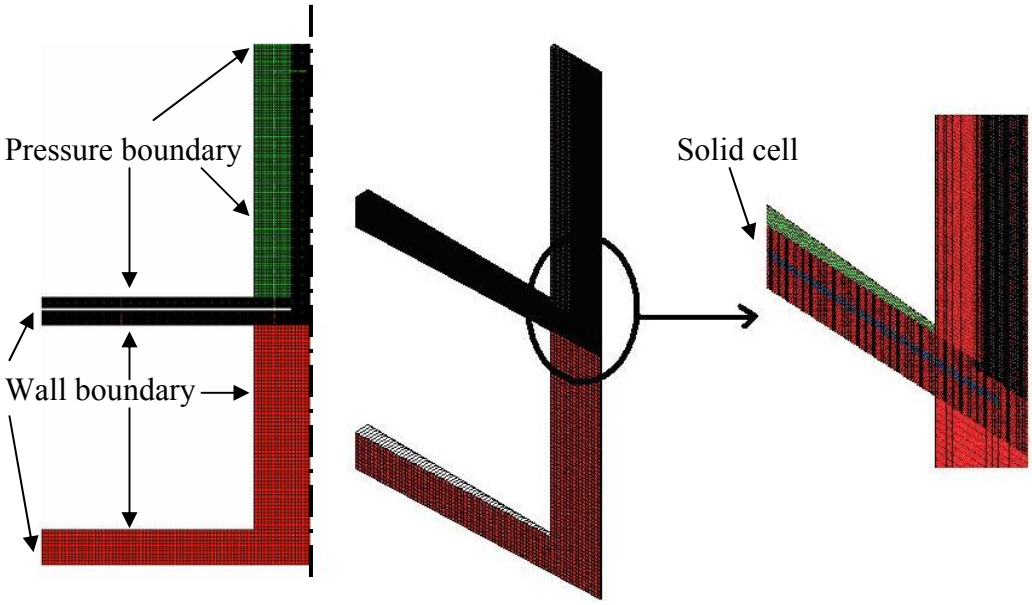

Fig. 4.2 Structured mesh of computational domain for droplet generator.

In Figure 4.3, a grid-independent solution was sought by evaluating the changes of the numerical solutions upon decreasing the grid size. The rms differences of solutions of 0.025 and 0.0125 mm grid sizes (compared at the same coordinates) are 1.32% for velocity, and 1.17% for pressure, and the maximum difference occurs at the filament neck, 1.88% for velocity and 1.65% for pressure along the interface line. Based on this, the grid size used in the model is taken as 2.5×10^{-5} m.

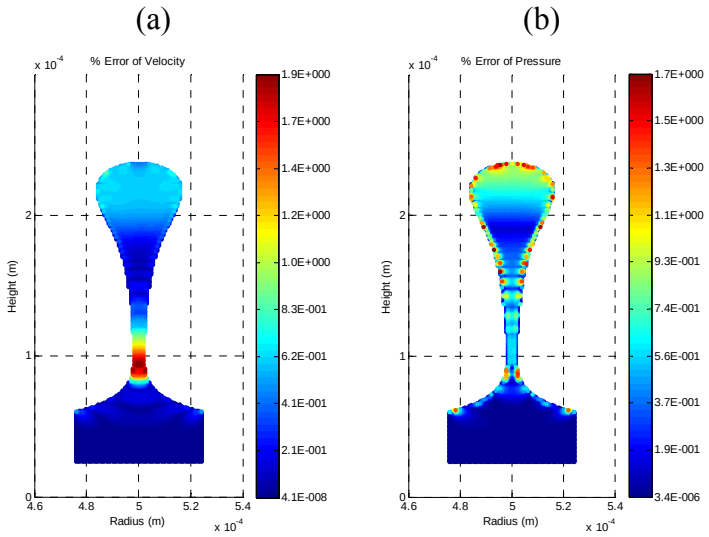

Fig. 4.3 Contour plots of the difference of two grid-size solutions: (a) velocity and (b) pressure.

Pinch-off Criteria

In this CFD simulation of droplet formation, the pinch-off criterion to determine a break-off is defined by the VOF fraction. During a necking process, the jet filament decreases in radius. When VOF fraction is less than 0.5 at the center-line cell along the liquid column, the break-off threshold is set. Based on this, the size of the filament is approximately 1.25×10^{-5} m, which is 1.25% of the nozzle diameter, when the break-off occurs, shown in Figure 4.4. James et al. [2003] use the same VOF value (0.5) to identify the break off with only 32 grids across the droplet (3.125%).

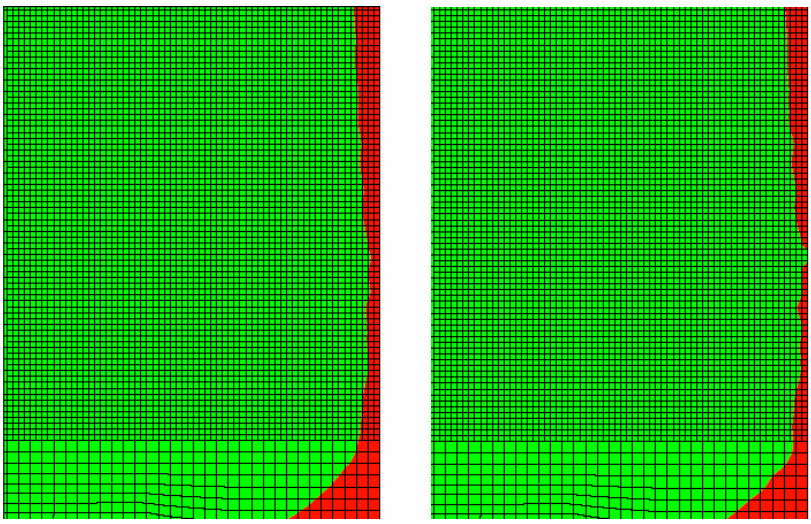

T = 2.800 τ = 2.825

Fig. 4.4 Pinch-off at the thread of fluid filament.

Fluid-structure interaction

The nonlinear large-deflection plate model is included in the CFD numerical computation by adding a user-defined subroutine to the CFD solver. In this subroutine, the pressure distribution on the nozzle plate is applied to the plate model to determine the actual displacement at every time step. Next, the deflection of a nozzle plate forms a new wall boundary used in fluid flow computation. Figure 4.5 shows how the fluid pressure interplays with plate deflection.

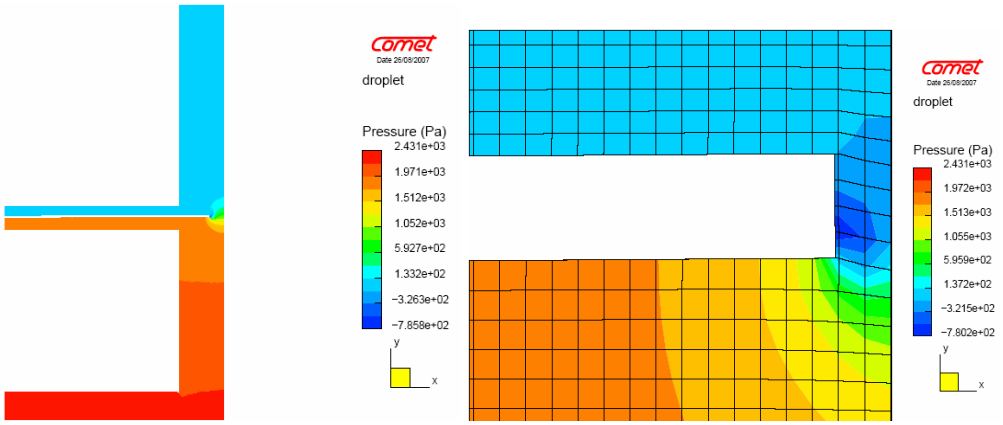

Fig. 4.5 Pressure distribution and fluid-structure-interaction inside the chamber.

4.3 SIMULATION OF DROPLET IMPINGEMENT

In droplet impinging, the surface tension force of the interface between the liquid phase and the solid surface is taken into account. This force affects the spreading and receding process. The normal of the interface of two immiscible fluids is determined by the gradient of the passive scalar c_l from Eqn. (16). Therefore, the contact angle at the interface is required as a boundary condition. A dynamic contact angle model is included to determine the local contact angle along the impinging process. In this work, the molecular kinetic theory model (M-K) is used to specify the dynamic contact angle.

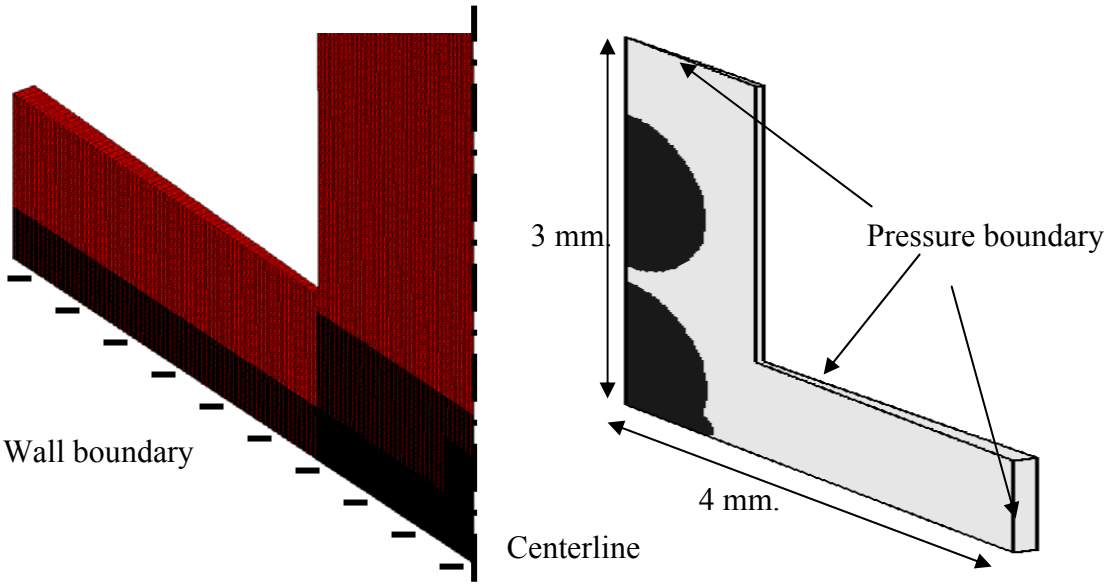

Fig. 4.6. Computational mesh and domain in three dimensional axisymmetric cylindrical coordinates

In the computational domain, the droplet impingement on a horizontal solid surface was modeled using a three-dimensional axisymmetric cylindrical mesh. Figure 4.2 presents the computational domain for the study of a droplet impingement. The computational domain extends to 4 mm in radius and 3 mm high using 50,000 wedged-like structured cells as shown in Figure 4.6. The finest mesh size, 0.01 mm, is assigned in the near wall region. To validate the numerical solution, two criteria were used to check the accuracy of the CFD model: grid-independent solution and experimental validation. The comparison with the experimental results is presented in the Results section. A grid-independent solution was sought by the reduction of grid size while evaluating the change of the numerical solutions. In Figure 4.7, the rms percentage difference of solutions between 0.01 mm and 0.005 mm grid sizes are about 0.11% for velocity and 0.18% for pressure. The maximum difference between the solutions is about 0.5 % for velocity which occurs near the solid surface and the interface between gas and liquid. The maximum difference of the pressure is 1.03% which occurs near the liquid-air interface.

(a) (b)

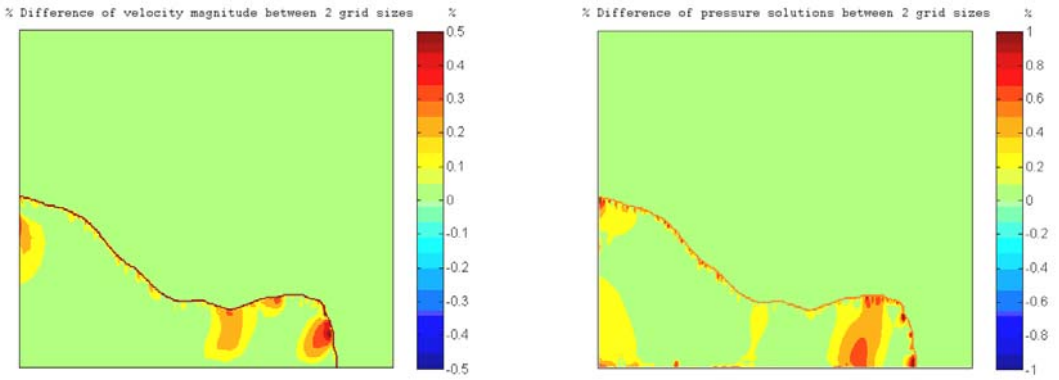

Fig. 4.7. Contour plots of the % difference of two grid-size solutions: (a) velocity and (b) pressure.

The M-K theory model is included in the CFD numerical computation by adding a user-defined M-K theory model to the CFD solver. In this user subroutine, the location of the edge of the droplet is recorded at each time step; the contact line velocity, U_{CL}, is determined by the difference of the contact-line location of two consecutive time steps as shown in Figure 4.8. Then, the known U_{CL} is used in the M-K theory model for the calculation of the dynamic contact angle. The contact angle determined from the M-K theory is prescribed in the CFD numerical solver as a boundary condition at the liquid-solid (solid wall) interface of the current time step.

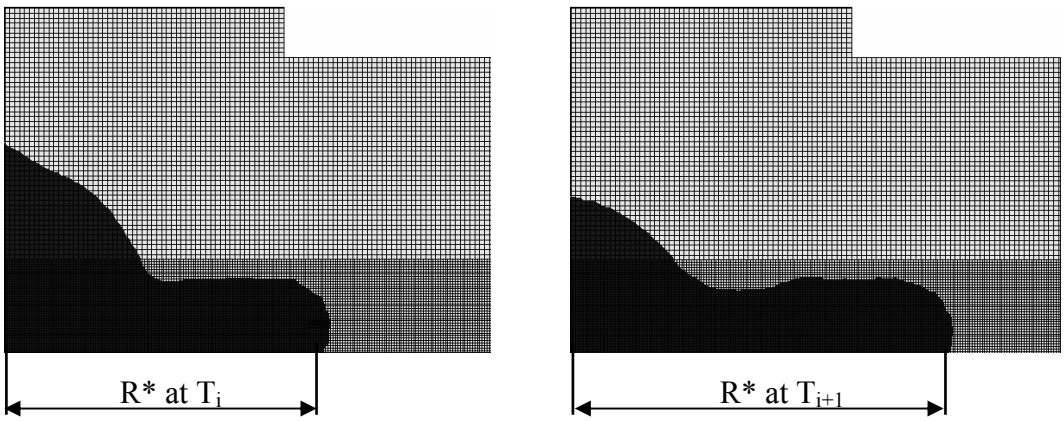

Fig. 4.8. Schematic of determining the contact line velocity.

CHAPTER 5

RESULT AND DISCUSSION

In this study, the numerical simulations are conducted for both droplet formation and droplet impingement by commercial CFD program. There are two major sections in this chapter: droplet formation and droplet impingement. In the droplet formation, the validation of the numerical solution by the experimental results is done by using a stiff nozzle plate condition. The different types of the excitation waveforms and input impulses are applied to the model to investigate their effects to the droplet formation characteristics. The variation of fluid properties is also studied. Later, the effect of a flexible nozzle plate is investigated along with the variation of fluid properties.

Next, the numerical simulation of single droplet impingent is validated with the experimental results. The equilibrium contact angles, successive impinging phases and fluid properties are varied to determine the spreading/receding characteristics of both single and successive droplet impingements.

5.1 DROPLET FORMATION

In this section, the results of the CFD simulations are validated with the experimental data from Hawke [2007]. Table 1 lists the geometric and fluid parameters used in this study. The results are presented in nondimensional form scaled by the capillary parameters as shown in Table 2. Table 3 shows the conditions of applied waveforms and vibrating characteristics of the nozzle plate on droplet formation. The prescribed displacement of the piezoelectric plate is considered as the input applied to the system to eject the droplet from the nozzle. Two types of piezoelectric waveforms are used in this study: step-function and

pulse- function. The difference of the outcomes between these two waveforms is significant, especially in the meniscus and resultant volume after break-off.

The nondimensional impulse (I*) is defined to represent the relation between the applied impulse and the droplet volume. I* is scaled by the system parameters indicating the size of the nozzle, total mass of fluid in the chamber, and piezoelectric diameter. The droplet formation using a flexible nozzle plate is discussed, focusing on the influence of plate vibration characteristics on the droplet formation. For different fluid properties, the droplet formation characteristics following break-off are changed such as droplet volume and velocity. For the computational experiments, the conditions of these two variables are listed in Table 4.

Table 5.1. Geometric and nominal fluid parameters of droplet formation.

Properties	**Value**
Nozzle hole radius, a: (μm)	1000
Nozzle plate radius, r : (μm)	15875
Nozzle plate thickness, h: (μm)	100 and 800
Density of fluid ρ: (kg/ m^3)	1000
Surface tension of fluid σ: (N/m)	0.074
Dynamic viscosity of fluid μ: (kg/m.s)	0.001

Table 5.2. Capillary scales using fluid properties from Table 1.

Variable	Description	Scale	Value
E_c	Stiffness	$\frac{\sigma}{a}$	148 Pa
l_c	Length	a	0.0005 m
P_c	Pressure	$\frac{\sigma}{a}$	148 Pa
t_c	Time	$\sqrt{\frac{\rho a^3}{\sigma}}$	0.0013 s
u_c	Velocity	$\sqrt{\frac{\sigma}{\rho a}}$	0.385 m/s
V_c	Droplet volume	$\frac{4}{3}\pi a^3$	0.524 mm^3

Table 5.3. Nominal nozzle plate characteristics with the driving piezoelectric waveforms; all cases use step-function waveform except case 2 which uses the pulse-function waveform. **Remark**: Nominal fluid properties shown in Table 1 are used for cases 1 through 9.

Case	h(μm)	E*	δ^*_{max}	τ_{rampup}
1	800	STIFF	0.17	4.51
2	800	STIFF	0.12	3.80
3	100	$3.38 \cdot 10^9$	0.183	1.54
4	100	$2.36 \cdot 10^9$	0.183	1.54
5	100	$1.35 \cdot 10^9$	0.183	1.54
6	100	$0.67 \cdot 10^9$	0.183	1.54
7	100	$0.34 \cdot 10^9$	0.183	1.54
8	100	$0.20 \cdot 10^9$	0.183	1.54
9	100	$0.07 \cdot 10^9$	0.183	1.54

Table 5.4. Nominal nozzle plate characteristics and fluid properties with the driving step-function piezoelectric waveforms

Case	σ*	μ*	E* (10^9)
10	0.5	1	E* = 0.07, 0.34, 0.67, 1.35, 3.38
11	2	1	E* = 0.07, 0.34, 0.67, 1.35, 3.38
12	3	1	E* = 0.07, 0.34, 0.67, 1.35, 3.38
13	1	0.5	E* = 0.07, 0.34, 0.67, 1.35, 3.38
14	1	2	E* = 0.07, 0.34, 0.67, 1.35, 3.38
15	1	4	E* = 0.07, 0.34, 0.67, 1.35, 3.38

5.1.1 Droplet formation with a stiff nozzle

This section discusses the validation of the CFD model and shows the base case results using a stiff nozzle plate. The comparisons of quantitative data and the shape of the liquid jet during the formation process are provided to validate the model. Based on the piezoelectric displacement responses given by Hawke [2007], the time dependent trace of the prescribed piezoelectric displacement is defined by Equation (20) below and plotted in Figure 5.1 for two input waveforms, a step function and pulse function defined in Equation (20). The nondimensional piezoelectric displacement is presented by the following time-dependent function where τ is the nondimensional time using the capillary time scale given in Table 2.

Step-function: Equation 20 (a)

$$\delta^*_{piezo} = \delta^*_{\max}\left(\frac{\tau}{\tau_{rampup}} - \frac{1}{2\pi}\sin\left(\frac{2\pi\tau}{\tau_{rampup}}\right)\right) \qquad 0 < \tau < \tau_{rmapup}$$

$$= \delta^*_{\max} \qquad \tau_{rmapup} < \tau$$

Pulse-function: Equation 20 (b)

$$\delta^*_{piezo} = \delta^*_{\max}\left(\frac{\tau}{\tau_{rampup}} - \frac{1}{2\pi}\sin\left(\frac{2\pi\tau}{\tau_{rampup}}\right)\right) \qquad 0<\tau<\tau_{rampup}$$

$$= \delta^*_{\max}\left(1+\left(\frac{1}{2\pi}\sin\left(\frac{2\pi(\tau-\tau_{rampup})}{\tau_{rampup}}\right) - \frac{\tau-\tau_{rampup}}{\tau_{rampup}}\right)\right) \qquad \tau_{rampup}<\tau<2\tau_{rampup}$$

$$= 0 \qquad 2\tau_{rampup} < \tau$$

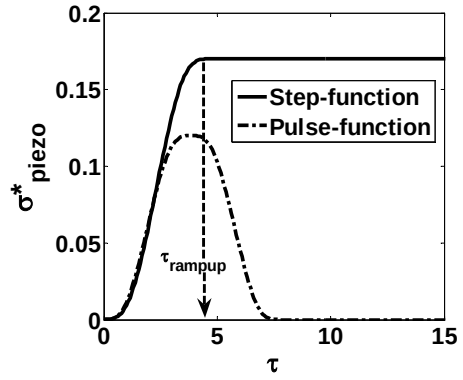

Fig. 5.1. Piezoelectric waveforms: step-function and pulse-function.

In Equation 20(a), the waveform is defined as a step-function with the rampup period from the rest position to the peak of the displacement. The main purpose of using this step-function waveform is to study how the total applied momentum would affect the formation of a liquid jet and the post-break-off droplet. The other waveform is a nondimensional pulse with τ_{rampup} = 3.80. This waveform given in Equation 20(b) is very close to the first one during the rampup interval, but after 5 ms (τ =3.80), the piezoelectric plate is forced to move back down to the initial position.

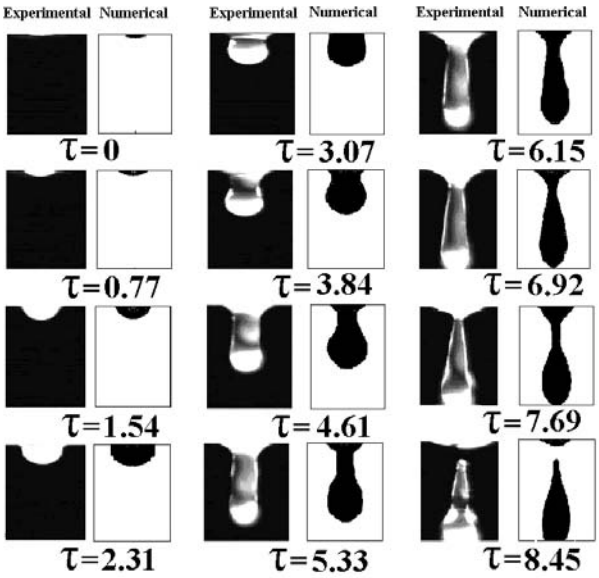

Fig. 5.2. Comparison between experiment images and numerical simulation contour plots of the step-function input with a stiff nozzle plate.

Figure 5.2 shows a series of images from the experiment and numerical simulation for the step-function case with the maximum piezoelectric displacement, δ^*_{max}, at 0.17 and the rampup time, τ_{rampup}, at 4.51 (case 1). During the rampup interval ($\tau < 4.5$), the protrusion of the liquid jet exiting the nozzle appears as a uniform column without necking because the piezoelectric continuously transfers its momentum from the driven waveform directly to the fluid inside the chamber. No negative suction or pressure occurs inside the chamber for the step-function waveform. For $\tau > \tau_{rampup}$, the piezoelectric stops and is held at its peak. During this time, the necking becomes significant. The neck of the liquid thread appears close to the nozzle exit and continues decreasing in radius while the leading edge propagates outward. At $\tau = 8.45$, the droplet breaks off from the main liquid column outside the chamber with a meniscus left at the nozzle exit.

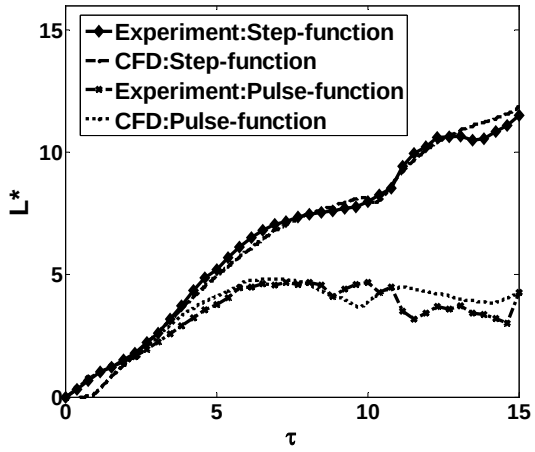

Fig. 5.3. Leading edge position, L*, versus time, τ, for both experimental and numerical simulation results.

Figure 5.3 is a comparison of experimental and numerical simulation results of the position of the droplet leading edge. Results include both functions. The step function results show a continual increase in position with a slowing of the leading edge right at break-off at $\tau = 8.5$ However, after break-off, there is "rebound" acceleration with oscillatory behavior and a second deceleration at approximately $\tau \sim 13$. The results of the step-function input show that most of the momentum produced by the piezoelectric motion causes the leading portion of the liquid jet to accelerate more than the rear portion. This is because the trailing portion of the fluid leaves after the rampup period when the piezoelectric is stationary. This causes the necking to occur near the nozzle and break-off to occur outside of the chamber but very close to the nozzle as shown in Figure 5.2.

The volume of the liquid column jetting out of the nozzle versus time is shown in Figure 5.4 for both waveforms. There is a discontinuous decrease of the volume that occurs right after break-off ($\tau = 8.5$ for the step-function waveform), this is because the volume only includes the droplet after break-off. The difference between the maximum volume and the droplet volume is the volume of the

meniscus left near the nozzle exit. For the step-function waveform from approximately τ = 4.5 to 8.5, the volume remains constant up to break off even though the leading edge is moving forward. This indicates a balance of forward moving fluid and necking with no net ejection of new fluid from the nozzle exit.

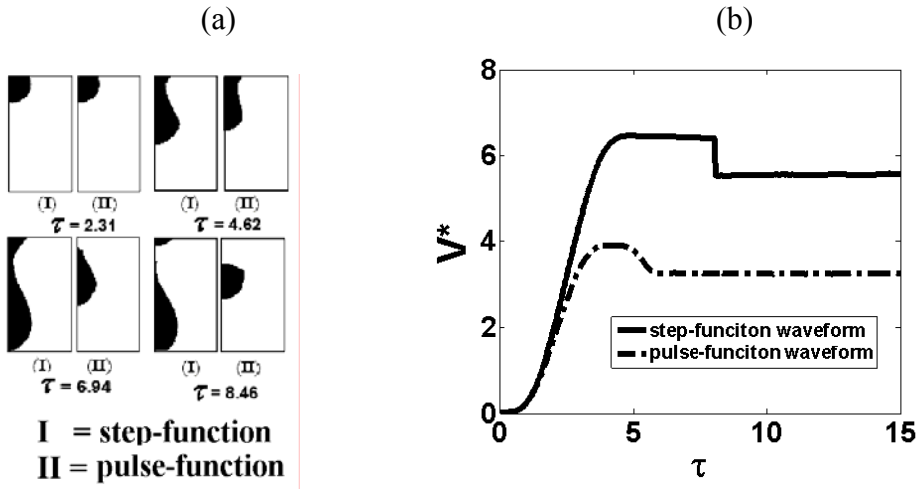

Fig. 5.4. (a) Droplet formation for the two different waveforms, and (b) volume of the liquid column and droplet after break-off.

Next, the pulse waveform is examined to determine whether the retreat of the piezoelectric causes any effect on the droplet formation process. From Figure 5.1, the pulse waveform has the piezoelectric reaching the maximum displacement (δ^*_{max} = 0.12) at τ = 3.80. The receding of the piezoelectric not only decelerates the propagation of the liquid column as shown in Figure 5.2, but also generates a suction pressure inside the fluid chamber. This suction pressure causes the leading edge to slow down and gradually move back towards the nozzle. The necking of the liquid filament occurs inside the fluid chamber and break-off happens at the nozzle exit, as shown in Figure 5.4 (a). The volume of the liquid column in Figure 5.4 (b) substantiates the meniscus receding back into the nozzle showing a decrease in the volume after τ = 3.81. The pulsed waveform results in a faster break-off time, τ = 6.5 versus τ = 8.5, for the step function, and a smaller droplet volume, by approximately 40%.

A nondimensional impulse function, I*, is introduced to define the ratio of the total impulse from the piezoelectric displacement at a single time step to the product of the total mass of liquid in the chamber and the capillary velocity which is based on the ratio of surface tension and nozzle hole diameter. Based on this, the expression for I* is:

$$I^* = \frac{\frac{1}{T_{rampup}} \int_0^{T_{rampup}} m_{displaced}(t) u_{piezo}(t) dt}{M_{reservoir} u_c} \tag{21}$$

where $\delta_{piezo}(t)$ = displacement of the piezoelectric, $u_{piezo}(t) = \dot{\delta}_{piezo}(t)$, $m_{displaced}(t) = \pi r_{piezo}^2 \delta_{piezo}(t)$

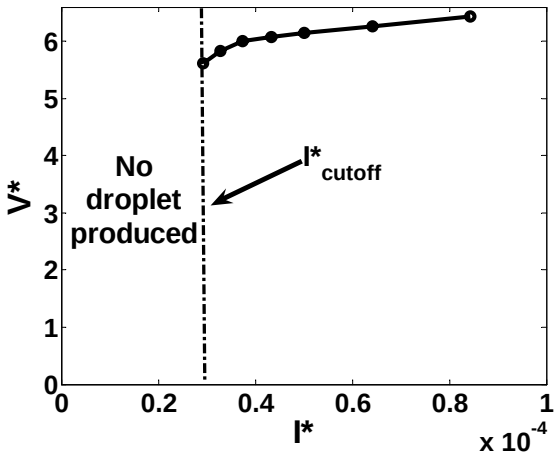

Fig. 5.5. Relationship between V* and I*, and the cutoff impulse.

In Figure 5.5, the relationship between nondimensional impulses I* and droplet volume V* is presented for the step-function waveform. There is a nearly linear relation between I* and V* at the high impulse region (I* > 0.4). The cutoff impulse occurs at I* = 0.3 below which there is no droplet break-off. This result is expected to be dependent on the droplet generator geometry.

5.1.2 Droplet formation with a flexible nozzle

The results of a passively vibrating nozzle plate are presented by comparing parameters such as droplet volume, velocity, break-off time, and pressure at the nozzle exit for several flexible nozzles with different values of Young's modulus.

As shown in Table 3, the nozzle-plate vibration is investigated using case numbers 3 to 9. For these seven cases, the applied waveform is a step function with total displacement $\delta^*_{max} = 1.5 \cdot 10^{-3}$ at $\tau = 1.45$. Figure 5.6 (a) shows the deflection of the nozzle plate at the nozzle exit versus τ. The smaller the Young's modulus, the larger the displacement. Moreover, the oscillating frequency of the plate response is also related to the flexibility of the nozzle plate, with a higher frequency response for lower Young modulus values. Figure 5.6 (b) shows the comparisons of the large-deflection plate model between the results from the CFD solution and the analytical closed-form solutions from Ugural [1981]. This solution is for a uniform applied pressure. So to compare results, the CFD pressure was averaged along the bottom of the plate and compared to a uniform applied pressure for the analytical solution. The CFD result shows good agreement with the analytical results; and also the distributed pressure condition has essentially no effect on the nozzle deflection compared to that of a uniform load.

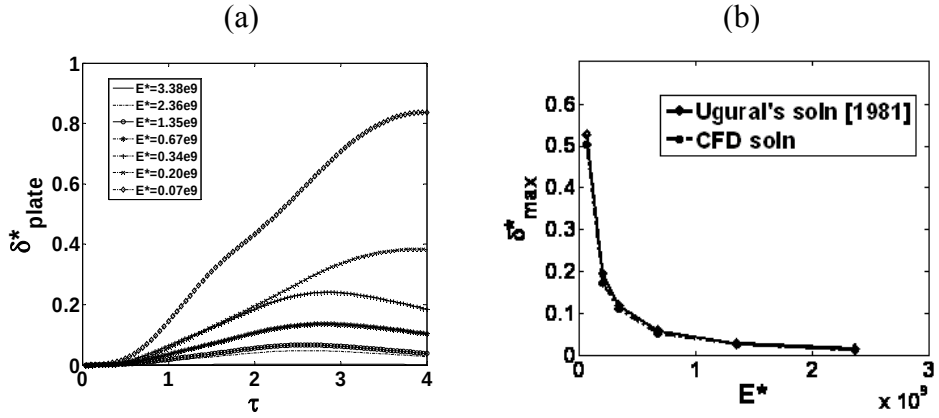

Fig. 5.6. (a) Nozzle plate response with respect to τ, and (b) validation of plate model with the solution given by Ugural [1981].

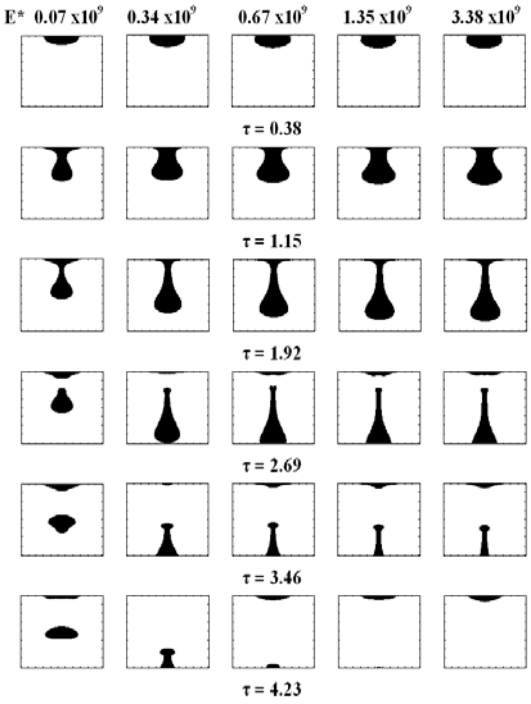

Fig. 5.7. Series of droplet formation for different values of E* for the nozzle plates at six different times after the activation of the piezoelectric diaphragm with $\sigma^*=\mu^*=1$.

A series of snapshots of the droplet formation process are shown in Figure 5.7 for different nozzle stiffness values. It is evident that the droplet formation from the more rigid nozzle plate (large E*) has a longer break-off distance and faster droplet velocity. The filaments for the more rigid plates become thinner quicker, resulting in longer filaments. Figure 5.8 shows the pressure just beneath the nozzle exit, the equivalent of one plate thickness below the nozzle exit for different values of E*. It is seen that the pressure rises quickly, decreases, goes negative, and then stabilizes. The ripple noted $\tau > 3$ is due to droplet break-off. By examining the detailed flow, it is found that the nozzle plate starts to deflect outward when the fluid inside the chamber is accelerated by the piezoelectric movement. The peak of each pressure profile occurs between $0.5 < \tau < 0.75$ with increasing magnitude of the pressure for increasing values of E*, since the higher values of E* have lower nozzle deflection. The time to reach the peak is approximately the same for each

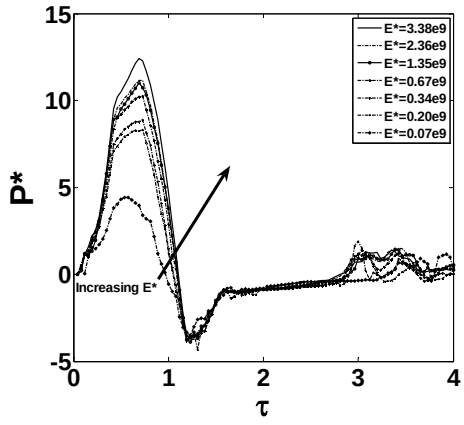

Fig. 5.8. Nondimensional pressure, P*, versus time, τ, for different values of nondimensional Young's modulus, E*.

case because this peak is reached well before the plate begins to recede, as shown in Figure 5.6. The pressure decreases with the expansion of the volume of fluid from the nozzle exit. For this reason, the pressure at the nozzle varies directly with Young's modulus. It should be noted that, for times $\tau > 1$, the negative pressure is created nearby the nozzle exit because the piezoelectric plate is decelerated to stop at its maximum displacement.

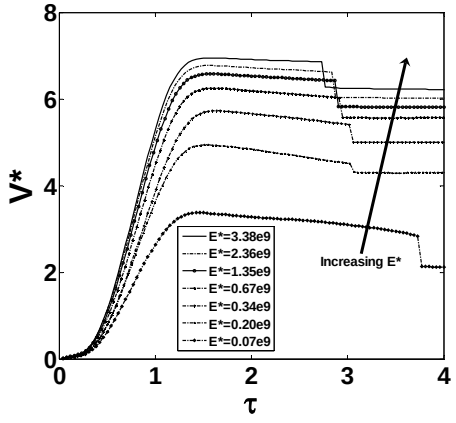

Fig. 5.9. Nondimensional droplet volume, V*, versus time, τ, for different values of nondimensional Young's modulus, E*.

The nondimensional volume, V*, of the liquid column ejected from the nozzle is presented in Figure 5.9 versus τ. For each nozzle plate stiffness, the fluid volume increases with time until a maximum is reached, and this time is essentially

independent of stiffness. The volume slowly decreases beyond the peak until a sharp decrease occurs. This decrease, which is largest for the more flexible nozzles, occurs at droplet break-off where only the separated fluid is included in V*. Comparing the P* and V* results, in Figure 5.8 and 5.9, it is apparent that the pressure has a significant effect on the volume of the droplet. The higher the maximum pressure at the nozzle exit, the larger the volume after break-off. The decrease of the volume of the fluid after the peak is more significant for the most flexible nozzles, indicating that more fluid retreats back into the nozzle the greater the plate deflection.

The trends of droplet formation parameters with respect to the values of nondimensional Young's modulus, E*, are given in Figure 5.10. There is a steep decrease of the break-off time for increasing values of E*, which corresponds to much larger droplet volumes. The volume of the droplet is shown to increase significantly with E*. For the most flexible nozzle, the droplet volume is approximately one-third of the volume for the stiff case. However, this trend is highly nonlinear, showing a large decrease in volume for very low values of E*. This rapid decline in droplet volume occurs when E* is less than 10^9. The velocity after break-off can be related to the pressure at the nozzle, which decreases with decreasing values of E*. Therefore as shown in Figure 5.10 (c), there is a significant decrease in velocity for the more flexible nozzle plate.

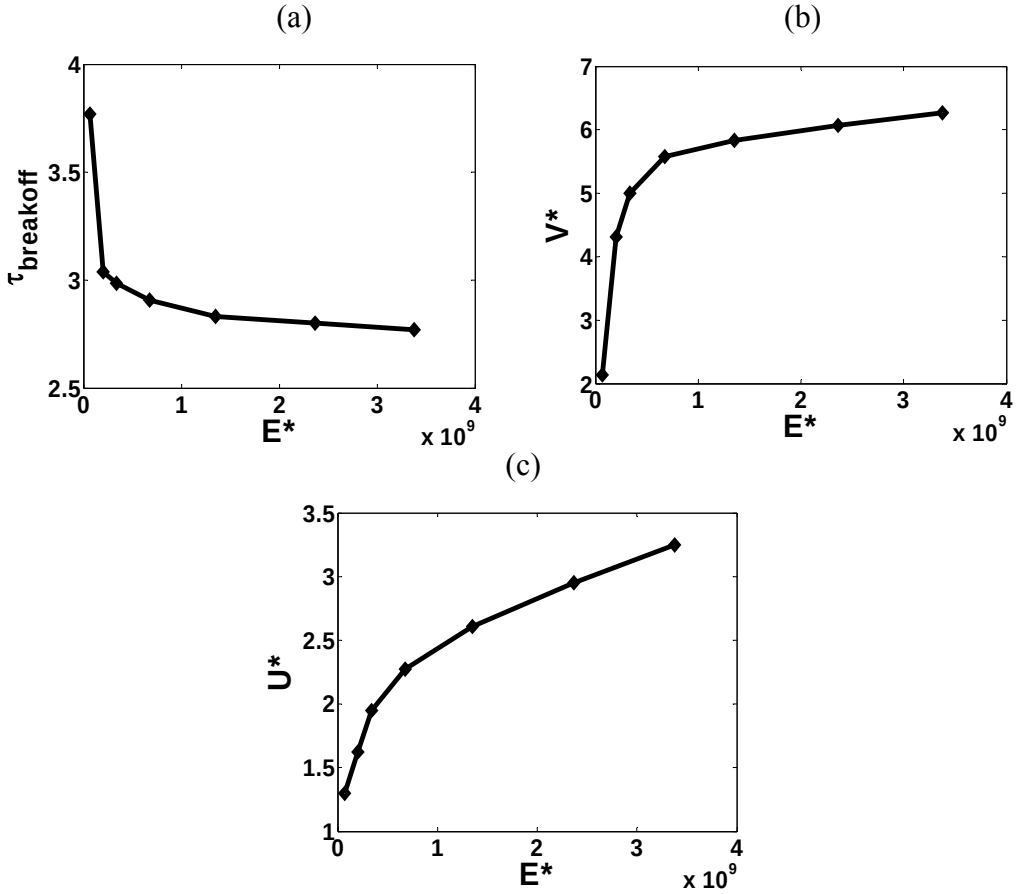

Fig. 5.10. Droplet formation flow characteristics versus E*: (a) break-off time, (b) droplet volume and (c) velocity.

5.1.3 Droplet formation with variation of fluid properties

The effects of fluid property variations on droplet formation were evaluated for surface tension and viscosity at different vibrating characteristics, E*. These cases are given in Table 4. The stiff nozzle condition was first evaluated using E* = 3.38×10^{9}. In Figure 5.11, a series of droplet formation images are presented for four different values of surface tension. The surface tension is defined by σ* which is the ratio of the fluid to water surface tension. At σ* = 0.5, the droplet after break-off has the highest volume and velocity compared with higher surface tension cases. For the very high surface tension case, the droplet volume more rapidly forms a shape without a trailing filament.

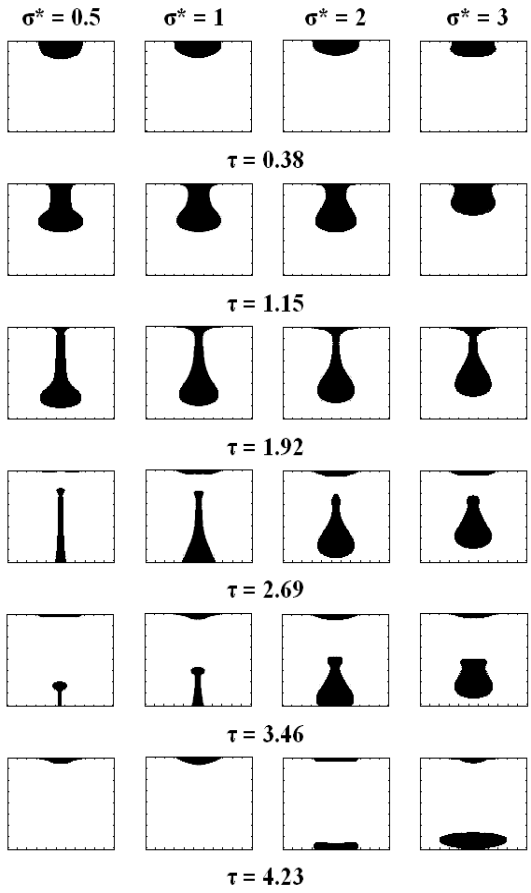

Fig. 5.11. Series of snapshots of droplet formation process for different σ* with μ*=1 and E*=3.38x10^9.

Figure 5.12 shows the droplet formation characteristics of the results for cases 10 to 13. Post-breakoff droplet volumes are presented in Figure 5.12 (a) Here, it is shown that there is no droplet break-off for the cases with the most flexible nozzle plate, E* = 0.07×10^9 when the surface tension is high, σ* ≥ 2. The droplet volume decreases almost linearly with surface tension. The droplet volume decreases faster with increasing surface tension as the stiffness of the nozzle plate decreases. Consequently, the combination of large plate flexibility and large surface force results in a large decrease in droplet volume. The post-breakoff droplet velocity is shown in Figure 5.12 (b) Results show a trend similar to the volume, as expected. For the case with σ* ≤ 1, droplet velocity is always greater than the capillary velocity even with the most flexible nozzle plate. Figure 5.12 (c) shows that the

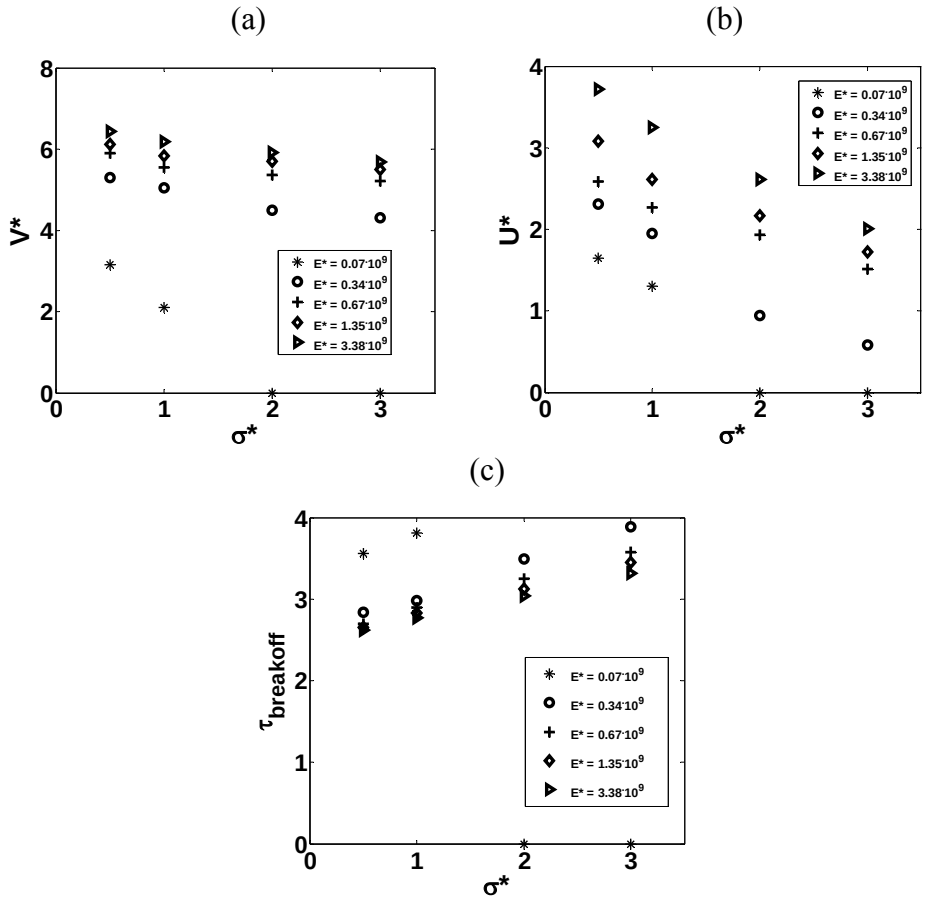

Fig. 5.12. Flow characteristics: (a) droplet volume, (b) velocity, and (c) break-off time versus σ*

increase in surface tension results in larger break-off times. Overall, the flexible nozzles enhance the ability to decrease droplet size and provide lower momentum drops as the surface tension increase.

For case 13 with E* = 0.07×10^9 and large surface tension, the droplet is not ejected from the nozzle due to the strong effect of surface tension and the lower pressure developed at the nozzle due to the large displacement of the nozzle plate. Figure 5.13 shows a series of images of the meniscus for the non-breakoff condition. It is obvious that the surface tension force deters the liquid jet from jetting out of the nozzle and later pulls the meniscus back to the chamber.

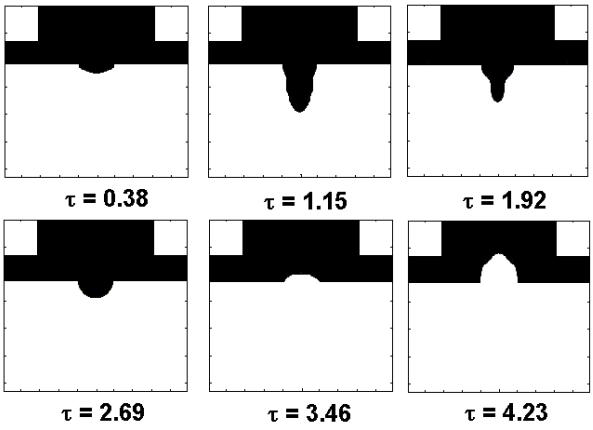

Fig. 5.13. Series of images for non-breakoff case with σ* = 3 and E* = $0.07 \cdot 10^9$

The effect of fluid viscosity on droplet formation is quantitatively presented in Figure 5.14 similar to Figure 5.12. The viscosity has a weak influence on the droplet formation process for the system being studied. Overall, increasing viscosity reduces droplet volume, but actually slightly increases droplet velocity. This combination results in essentially no change in droplet momentum. This consequence indicates that surface tension is the dominant fluid property in this process.

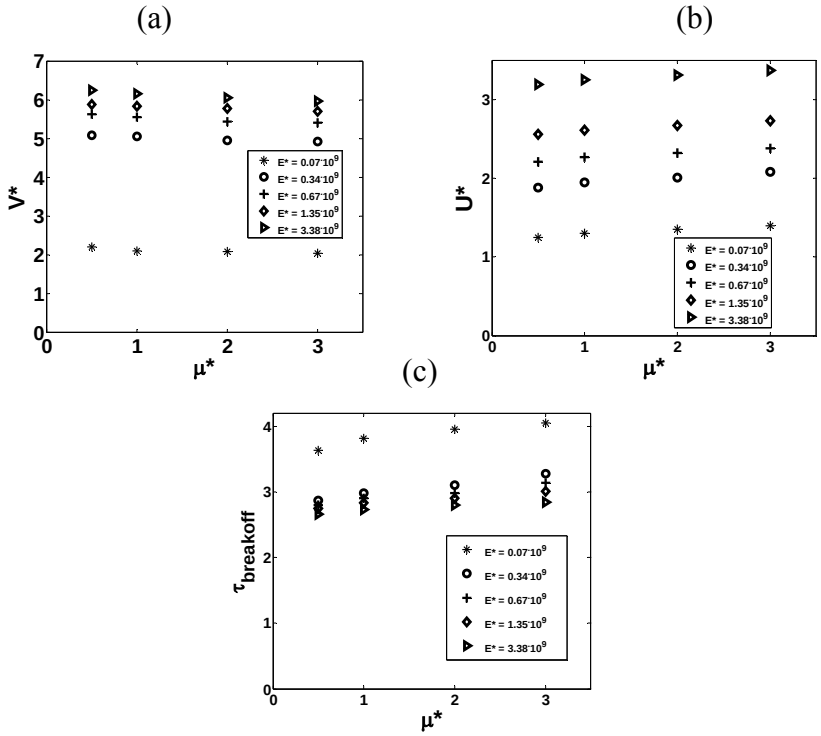

Fig. 5.14. Flow characteristics: (a) break-off time, (b) droplet volume and (c) velocity versus μ*

5.2 DROPLET IMPINGEMENT

In this section, the results of the simulations are presented along with validation with the experimental data from Hawke [2007]. Cases for a single drop, successive drops impinging at different phases of spreading for the first drop, and for different fluid properties are presented. The initial conditions and nominal fluid properties of the droplet are given in Table 4. Single droplet impingement on a solid flat surface using the M-K theory dynamic contact angle model is presented first and then followed by results for successive droplet impingement and results for a range of fluid property conditions.

Table 4. Geometric and nominal fluid parameters of droplet impingement.

Properties	**Value**
Pre-impact droplet radius, R_o: (mm)	0.55
Pre-impact droplet velocity, U_o: (m/s)	1.1
Density of fluid, ρ: (kg/ m^3)	998
Surface tension of fluid, σ: (N/m)	0.074
Dynamic viscosity of fluid, μ: (kg/m.s)	0.00114
Solid surface	Plexiglass
Experimental equilibrium contact angle, Θ_E	75^o

The simulation cases for both single and successive droplet impingement are divided into two parts for the variations of an equilibrium contact angle and fluid properties. In the first part, the equilibrium contact angle and the phase of successive droplet impingement are assigned as the varied variables. The equilibrium contact angle was changed from 45^o to 120^o at 15^o increments. The different time intervals between two successive drops are defined based on the phase of the first impinging droplet spreading: advancing, receding, and at rest. In

each phase of successive droplet impingement, $\Delta\tau$ is defined as the time interval between the impingement of the first drop and impingement of the second drop onto the first drop. The values of $\Delta\tau$ are 0.1, 2, and 12 for advancing, receding, and at rest phases respectively. For the cases focusing on the effects of fluid properties, σ^* and μ^* are used to define the ratio of fluid surface tension and viscosity to that of the nominal fluid, which essentially has properties of water. In each successive impinging phase, the nondimensional surface tension was varied as 0.5, 1, 2, and 3 for $\mu^*=1$. For the viscosity, μ^* was varied as 0.5, 1, 2, and 4 with $\sigma^*= 1$ for all cases.

5.2.1 Droplet impingement with dynamic contact angle

This section discusses the validation of the CFD droplet impingement model and shows the results with a single droplet impingement using the M-K theory model. The comparisons of quantitative data and the shape of the droplet during the impinging process are presented. Experimental results given by Hawke [2007] for a water droplet of 1.1 mm diameter with an impact velocity of 1.1 m/s hitting a Plexiglass surface were used to calibrate the M-K theory model. After impinging on the solid surface, the droplet spreads and reaches equilibrium with a 75 degree contact angle, which is considered a wettable condition. The nonlinear least square method was used to fit the data of measured dynamic contact angle and contact line velocity. This was used to determine κ_w and λ given in Equation 14. Shown in Figure 5.15, the optimal fitting of the experiment data is at $\kappa_w = 4.62\text{x}10^{7}$ and $\lambda = 6.25\text{x}10^{-10}$ with a root-mean-square and standard deviation error of the predicted contact angle of 9.23^{o} and 7.03^{o}, respectively.

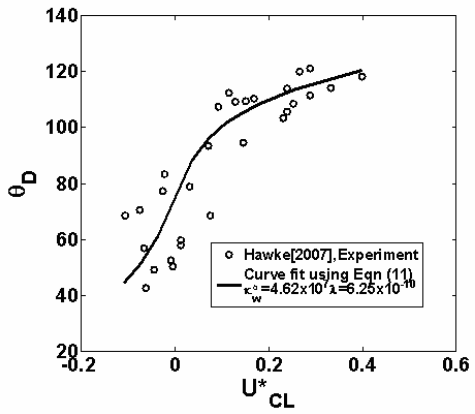

Fig. 5.15. Comparison of the dynamic contact angle, Θ_D, between experimental results and a least square curve fit using M-K theory model.

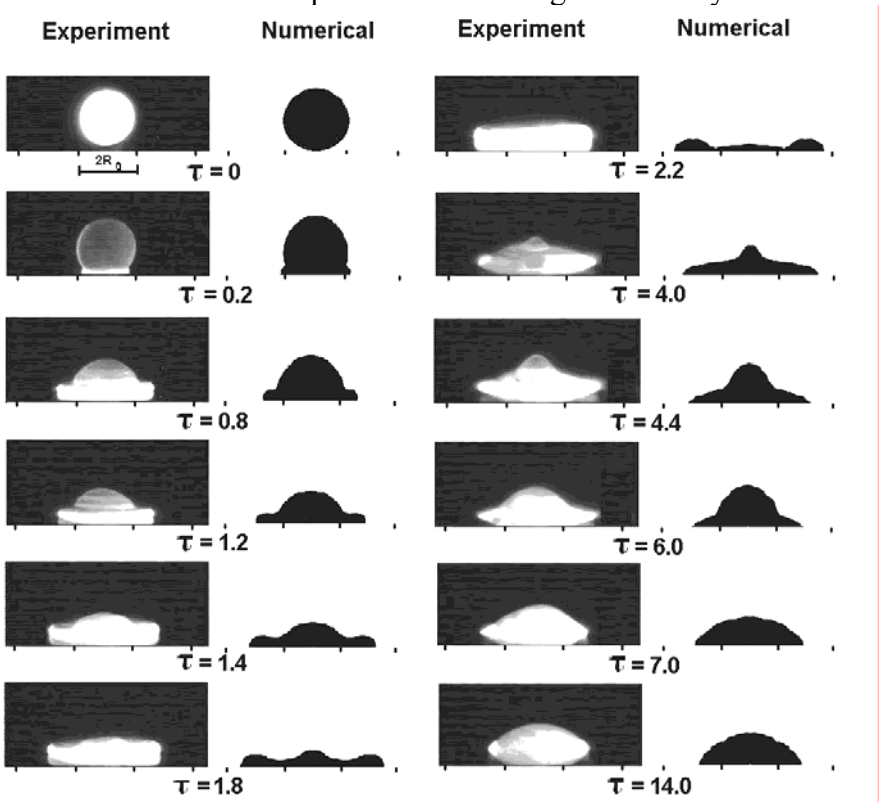

Fig. 5.16. Comparison of experimental data of Hawke [2007] and CFD results of the droplet impingement process for a single drop.

Figure 5.16 shows the experimentally obtained images of the shape of the droplet during the impinging process along with the CFD contour plots using the M-K theory dynamic contact angle model. The CFD simulation is able to capture most of the details in the impinging process. For the impinging process in Figure 5.16, the rim of the droplet is formed during spreading and the height of the

lamella, a dome-like thin film at the center of the impinging drop, starts to decrease. The spreading process stops as the droplet reaches its maximum spreading radius. After reaching its maximum radius, the droplet begins to recoil under the effect of surface tension forces. During the receding process, the contact angle at the outer edge is always less than the equilibrium contact angle due to the added momentum of the fluid near the receding contact line.

Figure 5.17 shows details of the velocity vector field in the region of the advancing and receding contact line for a single drop. During advancing, Figure 5.17 (a), a small recirculation region develops as fluid is drawn down towards the surface at the contact line. Once the droplet begins to recede, shown in Figure 5.17(b), fluid near the contact line flows back against the outward flow near the center of the droplet. The interaction between these two flows shows up as an upward flow which then turns back towards the center of the drop. Later during receding, shown in Figure 5.17 (c), the flow near the contact line becomes rather complex as the contact angle becomes very large because the viscous forces retard the flow near the surface, while the flow away from the surface has higher inward momentum.

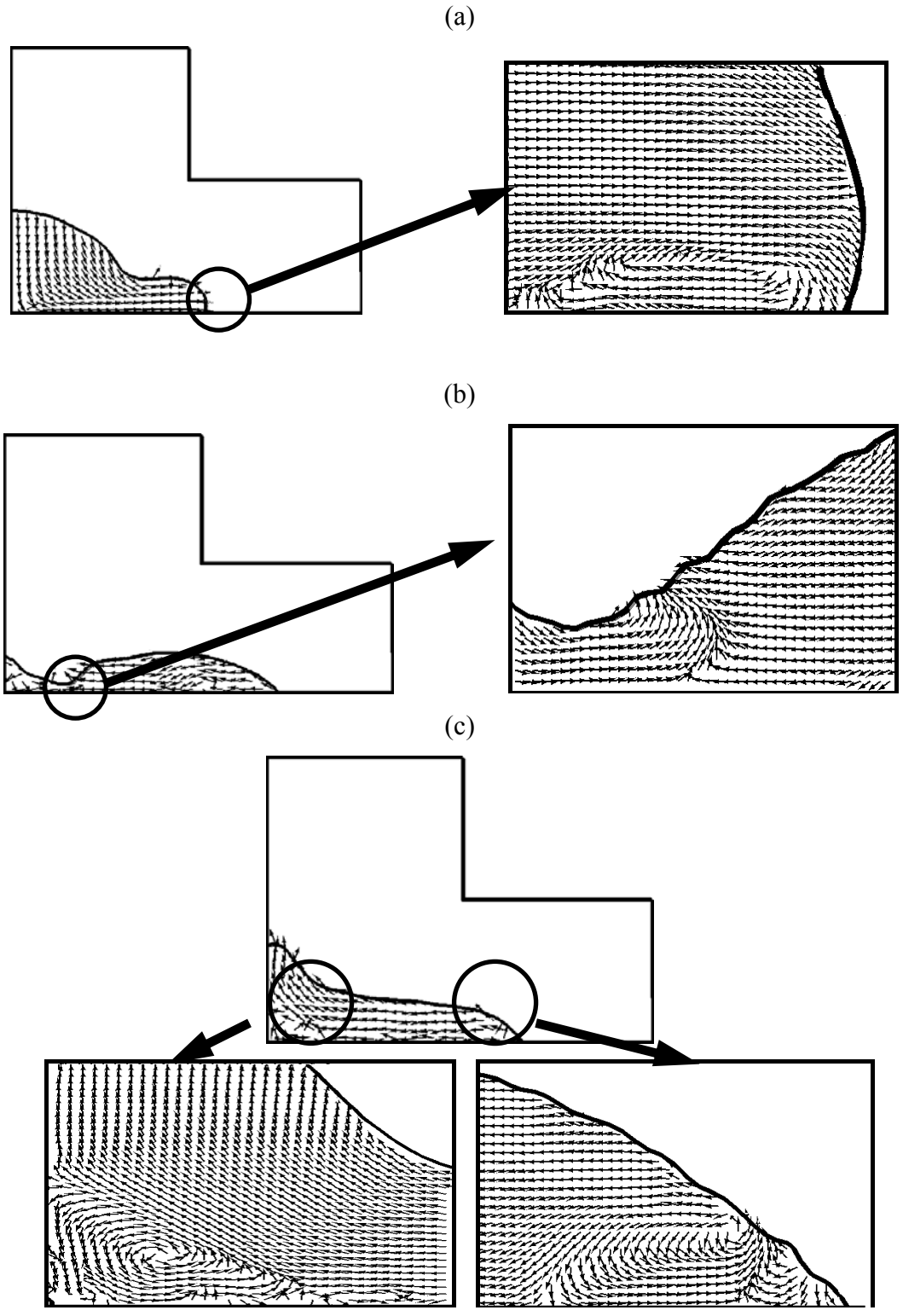

Fig. 5.17. Velocity vector field of the single droplet impingent with $\Theta_E = 75^o$, $\mu^*=1$, and $\sigma^*=1$; (a) advancing phase, $\tau= 0.6$ and $U^*_{CL}= 0.163$ advancing, (b) receding phase, $\tau= 2.2$ and $U^*_{CL}= 0.042$ receding, (c) receding phase, $\tau= 2.6$ and $U^*_{CL}= 0.067$ receding

5.2.2 Single droplet impingement under variation of equilibrium contact angle

In this study, it is assumed that both κ_w and λ in the M-K theory model are constant and valid for all equilibrium contact angles. Although this assumption has not been tested by experiments, a range of equilibrium contact angles were studied to determine the sensitivity of results on variations of this parameter. The investigation of the effect of the equilibrium contact angle was conducted using the single droplet impingement with a variation of an equilibrium contact angles. Figure 5.18, presents a series of snapshots of the droplet impingement at a series of times with different equilibrium contact angles. For a higher equilibrium contact angle, the spreading process forms a larger rim because of the higher surface tension forces which confines more fluid within the rim. In most of the cases, the maximum spreading radius is reached at $\tau = 1.8$ with varying sizes of the rim and lamella height. At $\tau = 3.4$ (receding phase), the case of $\Theta_E = 105^o$ has the highest lamella, the largest contact angle, and the smallest receding radius among the other equilibrium angles shown in the figure.

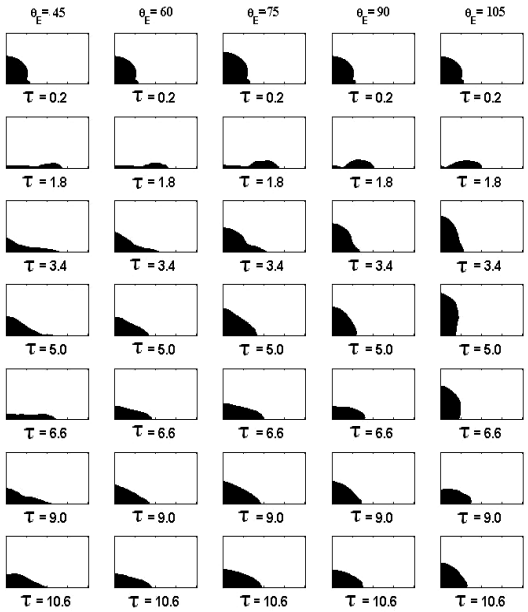

Fig. 5.18. Contour plots of the droplet impingement process for a range of values of equilibrium contact angle.

Results for the time-dependent spreading radius, R*, contact line velocity, U^*_{CL}, and dynamic contact angle, Θ_D, are given in Figure 5.19 for all cases of equilibrium contact angle studied. In Figure 5.19 (a), the greatest spreading radius occurs for $\Theta_E = 45^o$ (R* = 2.7) and the smallest spreading radius is for $\Theta_E = 120^o$ (R* = 1.8). For $\Theta_E = 45^o$, the receding phase propagates relatively slower than the other wettable cases ($45^o < \Theta_E < 90^o$). The higher the equilibrium contact angle, the further the droplet recoils. In Figure 5.19 (b), it is difficult to find major differences in the spreading velocity, because the trend and magnitude of each velocity profile are about the same except for small changes during rebound movement.

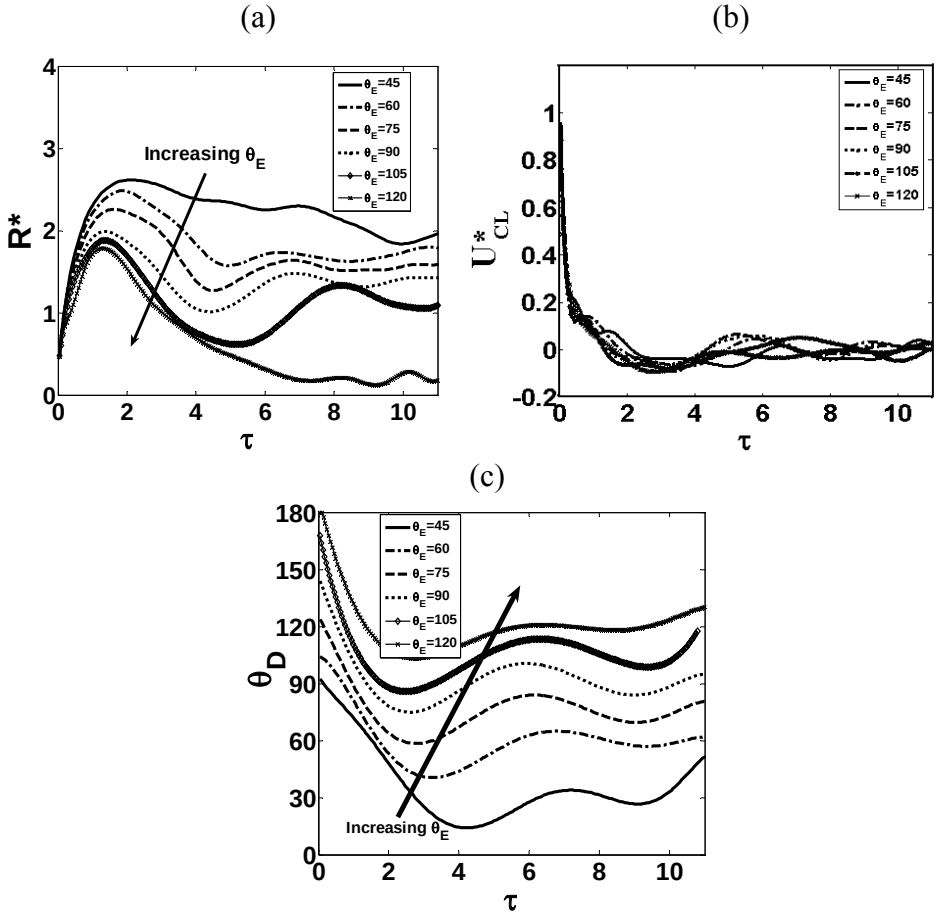

Fig. 5.19. Single droplet impingement parameters versus equilibrium contact angle, (a) R* vs τ, (b) U^*_{CL} vs τ, and (c) Θ_D vs τ.

When the droplet initially hits the solid surface, the dynamic contact angle is largest and then reduces while the droplet is advancing outwards, shown in Figure 5.19 (c). At the maximum spreading radius, the contact-line velocity is zero and the contact angle is equal to the equilibrium angle. The recoiling process starts suddenly and the contact angle decreases below the equilibrium contact angle due to the opposite direction of the contact-line velocity. At later times, the droplet spreading and receding processes oscillate back and forth for a few cycles until equilibrium is reached.

For the drops with different equilibrium contact angles, the levels of energy dissipation during spreading are different. The damping ratio of the first spreading-receding cycle for the wettable condition ($\Theta_E < 90^o$) is introduced to represent how the system dissipates energy during the impinging process. The damping ratio is expressed in terms of the ratio between the first two spreading radius peaks during oscillation. From Rao [1986], the damping ratio is then defined as:

$$C_\theta = \frac{1}{\sqrt{1 + \left(\frac{\pi}{\ln\left(\frac{A_2}{A_1}\right)}\right)^2}} \qquad (22)$$

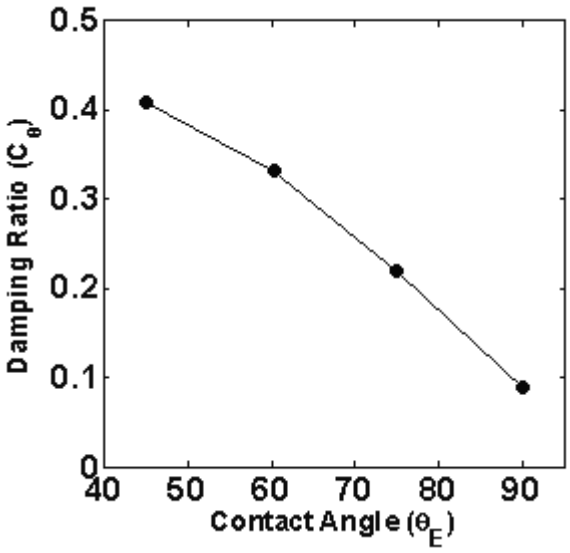

Fig. 5.20. Damping ratio vs. equilibrium contact angle for the wettable condition.

This damping ratio is based on the overshoot and undershoot magnitudes of the first cycle of the impinging process. From the simulations, the damping ratio for each equilibrium contact angle was determined and is presented in Figure 5.20. The drop with the lowest equilibrium contact angle (Θ_E = 45^o) has the highest damping ratio; this system dissipates kinetic and surface tension energies faster and reaches its equilibrium state sooner than the other cases. In Figure 5.20, the relationship between the damping ratio and the equilibrium contact angle shows an essentially monotonically decrease.

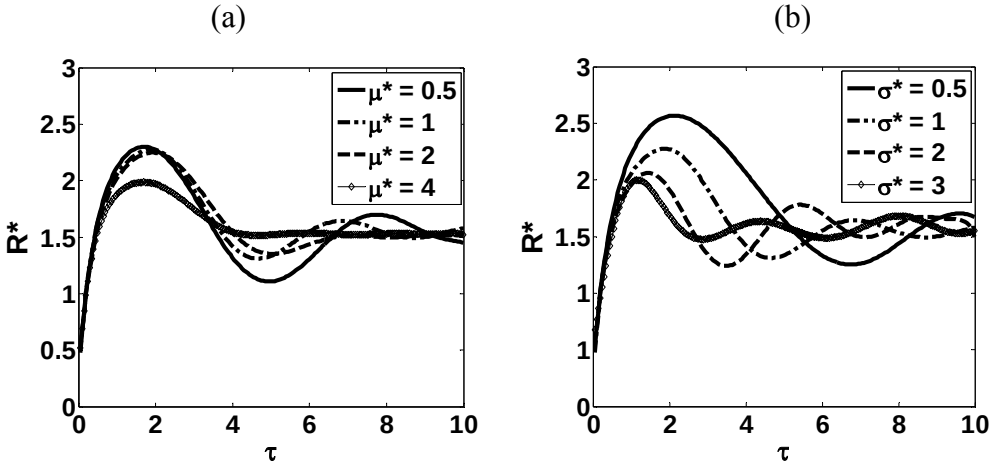

Fig. 5.21. Nondimensional droplet radius during impingement for different (a) viscosities and (b) surface tensions.

5.2.3 Single droplet impingement with variation of fluid properties

The effects of viscosity and surface tension, normalized by the nominal fluid value (water) are shown in Figure 5.21 for an equilibrium contact angle of 75^o. Increasing the fluid viscosity dampens spreading as well as the oscillation amplitude. In fact for the case of the viscosity four times greater than that of water there is no rebound spreading after the first recession and the droplet forms its equilibrium conditions very rapidly. For increasing surface tension, shown in Figure 5.21 (b), the oscillating amplitude and period are both decreased

significantly. These results indicate that a combined effect of increasing viscosity and surface tension will result in non-oscillating droplet impingement with a time scale for reaching static equilibrium approximately two to four times the capillary time scale.

(a) (b)

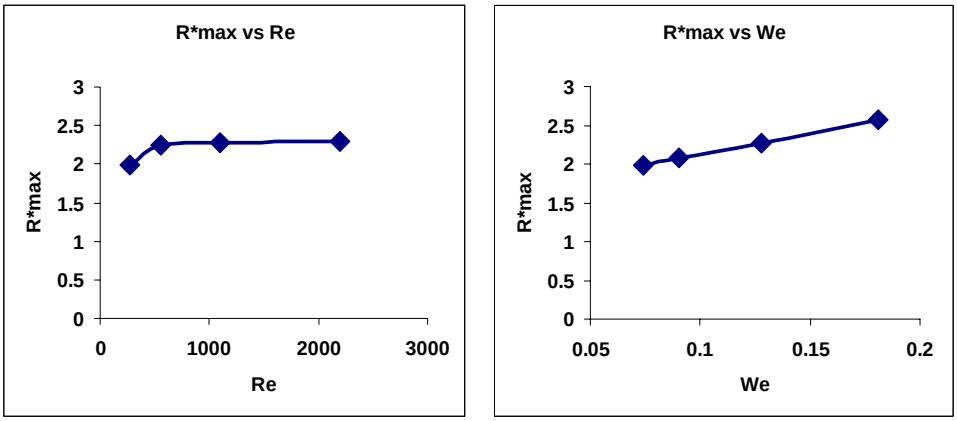

Fig. 5.22. (a) Re vs R*max, and We vs R*max.

For the study of the effect of fluid properties on droplet impingement, the relation between both Reynolds and Weber numbers with the spreading conditions are investigated. Figure 5.22 (a) presents the relation between the Reynolds number and the spreading rate. Here it is shown that the maximum spreading radius does not change significantly when Re is higher than 500. A large decrease in the maximum radius occurs at very low Reynolds number. Consequently, the value of viscosity have to be very high to affect the spreading process. In contrast to viscosity, the surface tension obviously has a linear relation to the maximum spreading radius as shown in Figure 5.22 (b).

The results of the maximum spreading radius during oscillations versus variations in fluid properties are represented in Figure 5.23 in terms of $(ReWe)^{1/2}$, where Re and We are the Reynolds number and Weber number, respectively, based on the impingement velocity and droplet radius. Although the results may not indicate a well defined mathematical trend, it is apparent that there is a increasing nearly linear trend, with a standard deviation of the curve fit of 5.42%. It should be noted that other combinations of Re and We were attempted with none yielding any definite trend. Since in this study only viscosity and surface tension were varied this result shows that a combined variation of viscosity times surface tension squared (as is the case for $(ReWe)^{1/2}$) shows an inverse relationship with the maximum spreading.

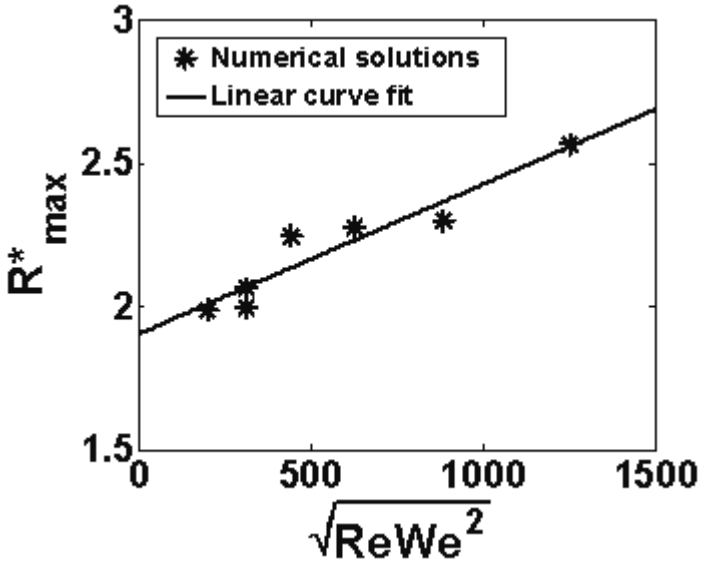

Fig. 5.23. Maximum spreading ratio vs $\sqrt{\mathrm{Re}\,We^2}$, and its curve fit for the trend of the data.

5.2.4 Successive droplet impingement under variation of equilibrium contact angles

In this section, the numerical results of successive droplet impingement are presented by comparing results from spreading and receding radii of four different phases of successive droplet impingement. The main objective of varying the timing of the successive droplet impingement is to study how the phase of successive impingement could affect the spreading and receding cycle of successive droplet impingement. Series of droplet profiles for four cases of droplet impingement processes at $\Theta_E = 75^o$ are shown in Figure 5.24 at different impinging phases along with a single drop. The main processes shown are pre-successive-impinging, liquid-liquid collision, surge of spreading, and receding.

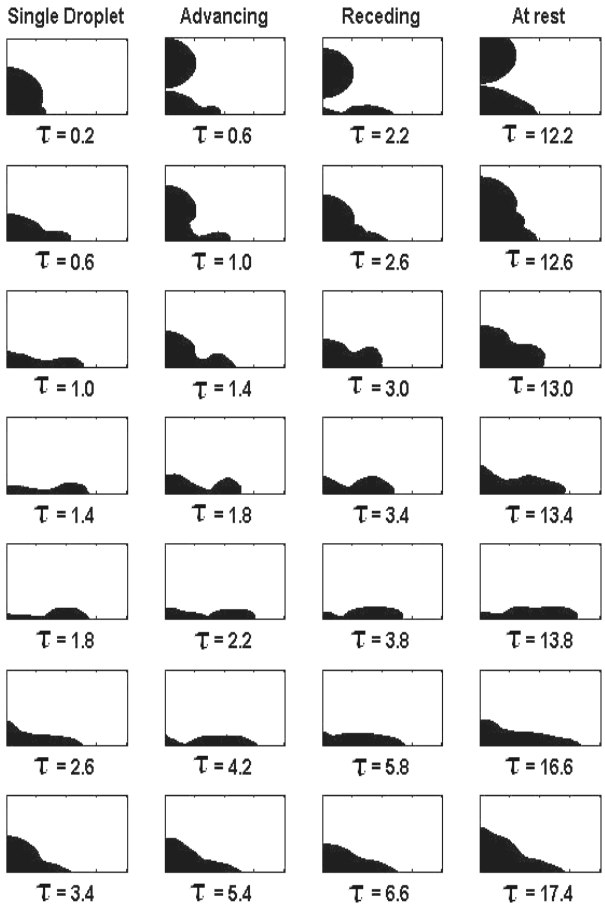

Fig. 5.24. Series of images during spreading with $\Theta_E = 75$ for single drop and successive drop impingement for different impinging phases.

For the case of successive impingement during first droplet advancing, the inter-droplet time interval is chosen as $\Delta\tau = 0.1$. The lamella of the first droplet is still high and the rim is not yet well-formed when the second droplet impinges on the first droplet. The momentum from the second droplet causes a surge in the spreading radius, adding momentum from successive impingement to the outward-driving momentum of the first droplet. For the case of the first droplet receding when impingement occurs, $\Delta\tau = 2$, the first droplet is forming a small lamella with a completely-formed rim around the outer edge of the droplet, when the successive droplet impinges. In the later stage, at $\tau = 2.6$, the rim disappears because of the recoiling of the contact line. However, the lamella is increased due to the successive droplet. At successive impingement, the direction of the contact-line displacement is suddenly reversed; the edge of the droplet is spreading out again due to the impact from the successive droplet. However, the momentum from the successive impingement is somewhat lower because of the interaction with the opposite-direction momentum from the receding of the first droplet. The successive impingement on a static droplet is also investigated. The momentum from liquid-liquid interaction drives the droplet spreading. The impinging process is almost identical to the single droplet impingement case except that the lamella and rim are approximately twice the height. However, as expected, the spreading radius has a larger advancing distance than the single droplet case, but not twice as large.

The above mentioned effects are shown quantitatively in Figure 5.25, which plots the spreading radius (R^*) of the outer edge of the droplet versus nondimensional time for three different cases of successive impingement. The successive impingement during the advancing phase has the greatest maximum

spreading radius, and the successive impingement on the receding phase has the smallest spreading radius. However, the difference is not large and the rebound seems to be essentially the same with the expected phase shift.

Detailed velocity vector fields are given in Figure 5.26 at different times for impingement during the advancing phase of the initial droplet. Details near the contact line are also given for the latter two times. The ridge is seen to have a fairly complex flow with recirculation on both the bottom and top portions of the ridge. The bottom one is a consequence of viscous forces and the top a consequence of interaction of high and lower momentum fluids. There is significant vertical flow compared to the single droplet advancement as higher momentum is provided by the impingement of the successive drop, accelerating the fluid into the ridge region. This type of complex recirculating flow may prove to be important in surface transport phenomena with impinging droplets.

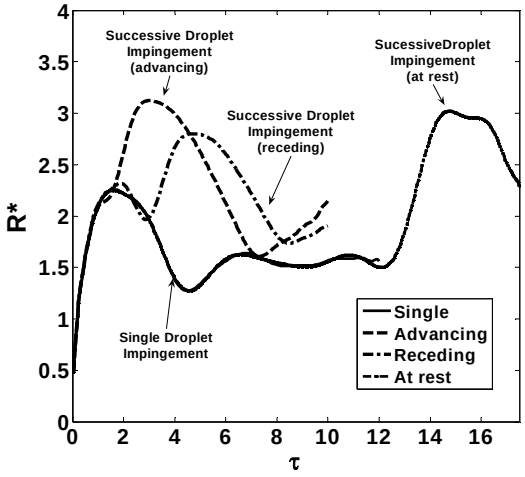

Fig. 5.25. R* vs. τ at four different phases of successive impinging, $\Theta_E = 75^o$.

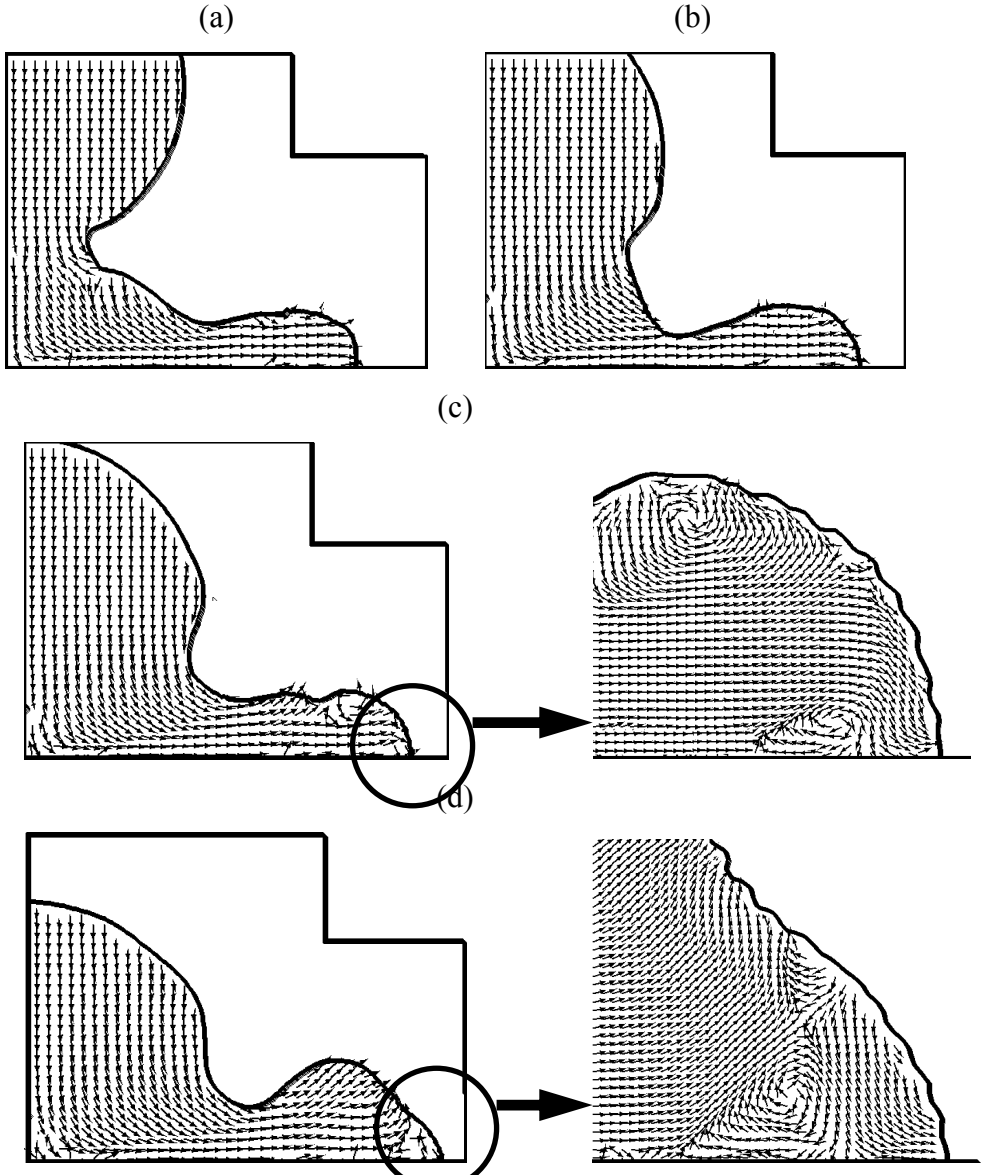

Fig. 5.26. Velocity vector field of successive impingement during the advancing phase with $\Theta_E = 75^o$, $\mu^*=1$, and $\sigma^*=1$; (a) $\tau = 0.8$,$U^*_{CL}= 0.244$, (b) $\tau = 1.0$, $U^*_{CL}= 0.166$, (c) $\tau = 1.2$, $U^*_{CL} = 0.123$, and (d) $\tau = 1.4$, $U^*_{CL} = 0.11$.

The velocity vector field successive impingement during the receding phase of the initial droplet is shown in Figure 5.27. Compared to the results shown in Figure 5.25 of impingement during the advancing stage the droplet shape is very different. The interaction of the receding phase with the second droplet causes a secondary bulge to occur which propagates outward and eventually forms into the ridge, which is much larger than that of the advancing impingement case. There is little or no recirculation in the ridge.

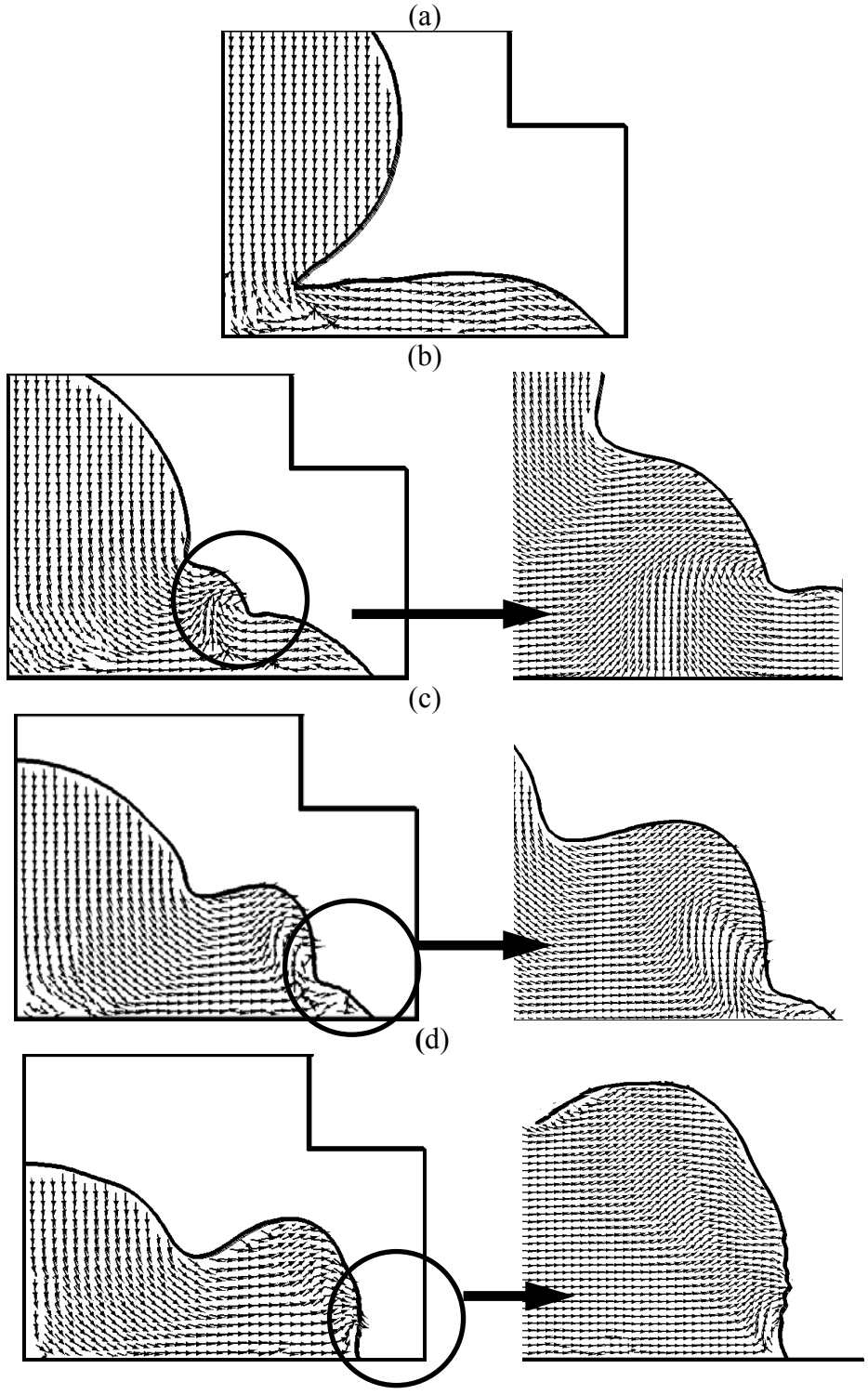

Fig. 5.27 Velocity vector field of successive impingement during the receding phase with $\Theta_E = 75^o$, $\mu^*=1$, and $\sigma^*=1$: (a) $\tau = 2.4$, $U^*_{CL}= -0.083$, (b) $\tau = 2.6$, $U^*_{CL}= 0.041$, (c) $\tau = 2.8$, $U^*_{CL} = 0.082$, and (d) $\tau = 3.0$, $U^*_{CL} = 0.123$

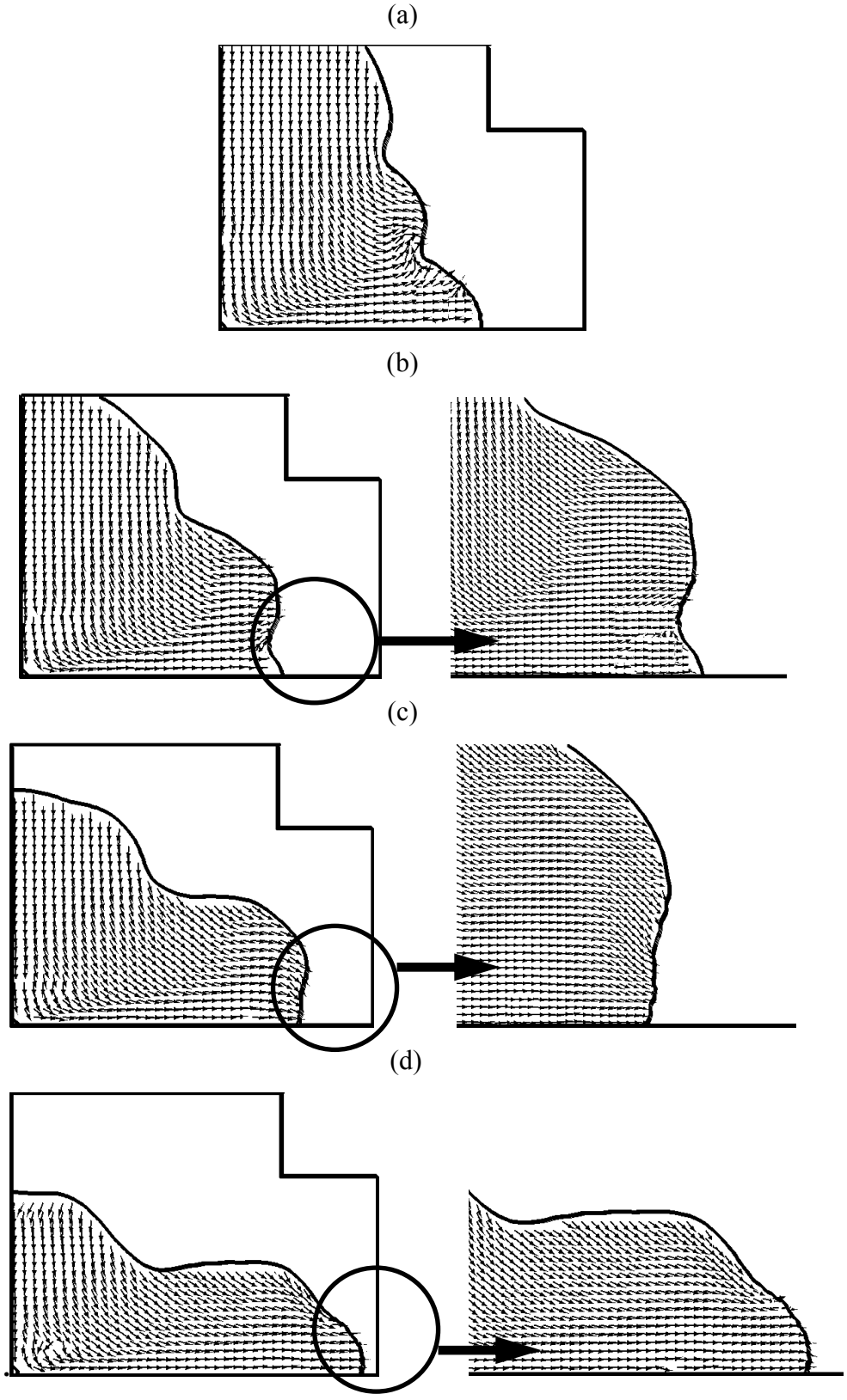

Fig. 5.28. Velocity vector field of successive impingement during the at-rest phase with $\Theta_E = 75^o$, $\mu^*=1$, and $\sigma^*=1$; (a) $\tau = 12.6$, $U^*_{CL}= 0.018$, (b) $\tau = 12.8$, $U^*_{CL}=0.101$, (c) $\tau = 13.0$, $U^*_{CL} = 0.159$, and (d) $\tau = 13.2$,$U^*_{CL} = 0.210$.

Final velocity vector field data is given in Figure 5.28 for the case of successive impingement when the initial drop is at static equilibrium. In this case the advancing fluid in the successive drop accelerates the initial droplet fluid outward, with a secondary ridge forming on top of the initial droplet. In this case there is very little or no recirculation that occurs. It should be noted that the contact line is moving faster than the bulk fluid in the ridge during the latter phases of spreading resulting a relatively thinner spreading layer than if this were a single droplet with twice the volume of the initial droplet.

The effect of the equilibrium contact angle on successive droplet impingement is shown in Figure 5.29. These plots show the spreading radii of successive droplet impingement at three different phases of the impinging droplet: advancing, receding, and equilibrium, with six different equilibrium contact angles. Note that in Figure 5.29 (c), the plot of the spreading radius for $\Theta_E = 120^o$ is not given because the equilibrium time for the initial droplet is much longer than the other cases. For the advancing case shown in Figure 5.29 (a), the droplet spreading surges outward after successive droplet impinging. Moreover, the trend of the spreading characteristics is the same as for single droplet impingement in which the largest spreading radius occurs for the smallest equilibrium contact angle. For the case of $\Theta_E = 45^o$, the maximum spreading radius is almost twice that of the single droplet impingement case. On the other hand, at $\Theta_E = 120^o$, the successive droplet impingement has a small effect on the spreading process in that it increases the spreading radius by about 20%. Figure 5.29 (b) presents the spreading radius of the receding-phase successive droplet impingement. It is seen that the additional momentum from the successive drop can increase the spreading radius by approximately 30% of the largest first-cycle spreading radius for the receding-

phase successive impingement. Moreover, at the higher equilibrium contact angle, this enhanced spreading decreases. In Figure 5.29 (c), the first droplet is static when the successive drop impinges on top of it. The trend of this case is essentially the same as the other two cases with the largest spreading radius less than the advancing-phase case, but slightly larger than the receding-phase case.

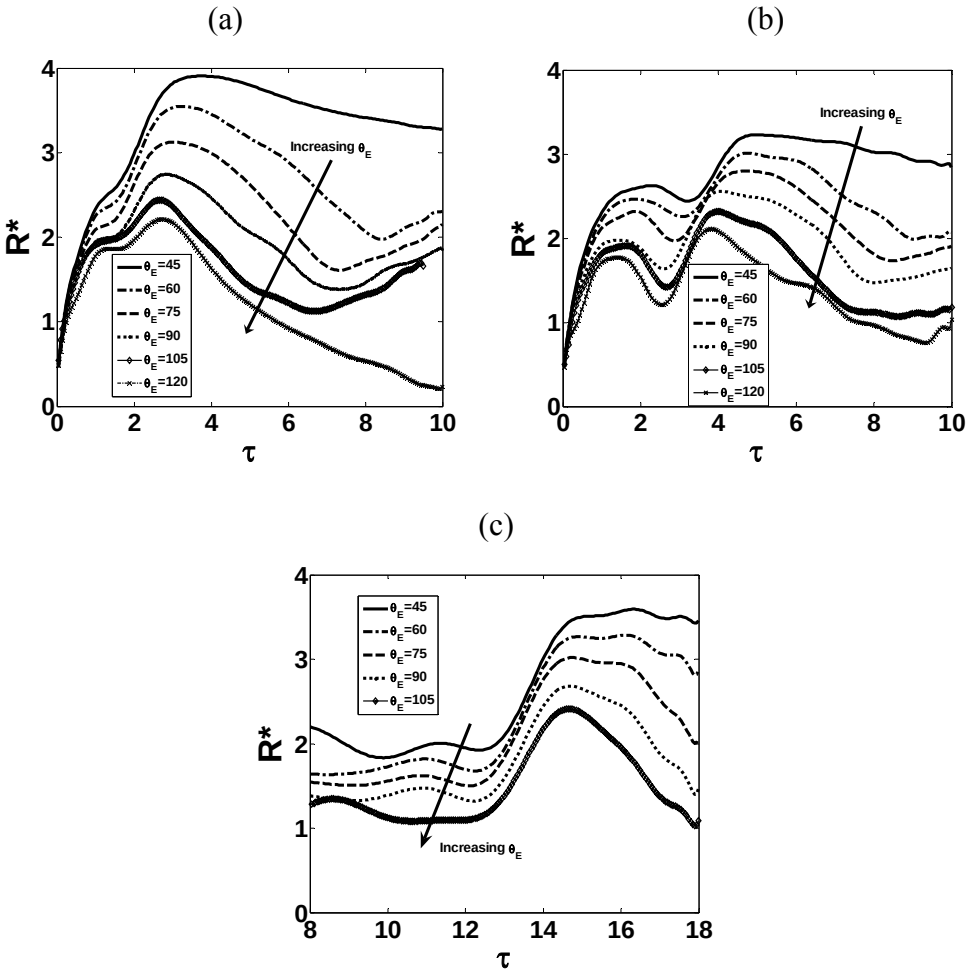

Fig. 5.29. Droplet impingement radius, R*, vs. τ for successive impingement at three different phases of the initial droplet; (a) advancing, (b) receding, (c) at rest.

Figure 5.30 (a) provides a measure of the effects of the equilibrium contact angles on the successive droplet impingement by plotting the maximum spreading radius versus successive impingement phase. Successive impingement during the

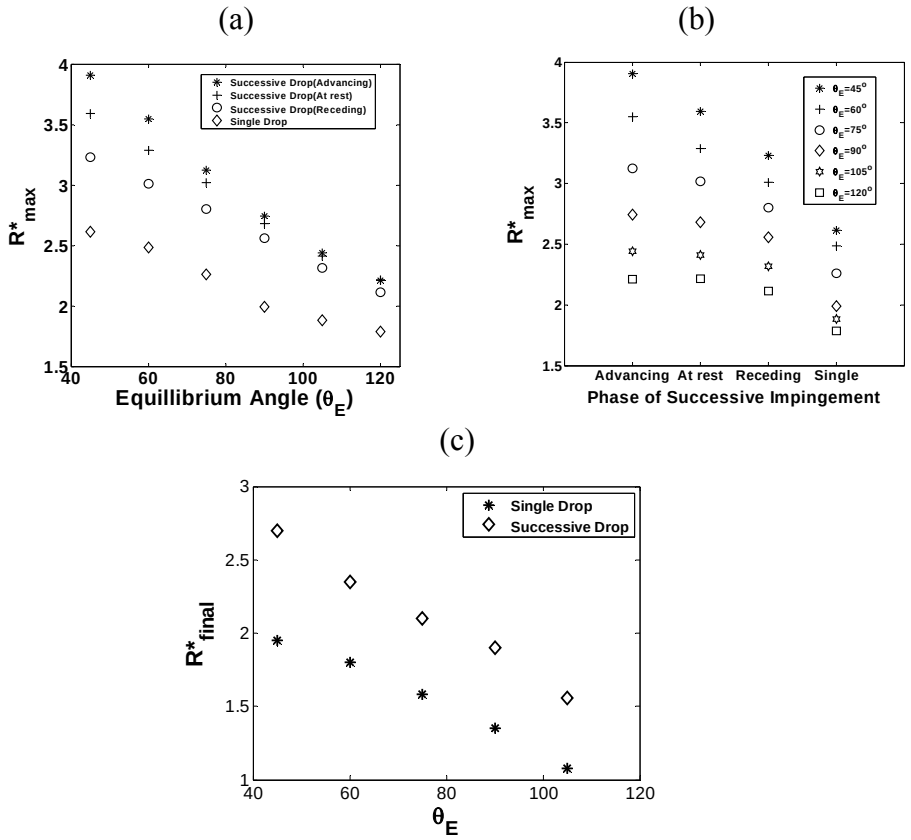

Fig. 5.30. Successive droplet spreading radius, R^*_{max} vs (a) equilibrium contact angle, (b) phase of the first impinging droplet subjected to successive impingement, (c) final radius of the at-rest droplet.

advancing phase has the greatest advancing radius (R^*_{max}). For the nonwettable cases ($\Theta_E > 90^o$), the phases of the successive impingement do not have as much of an effect on the maximum spreading radius (R^*_{max}). Figure 5.30 (b) shows the relationship between the phases of successive impingement and the maximum spreading radius (R^*_{max}) of each equilibrium contact angle. For the case of high wettability ($\Theta_E < 90^o$), the phase of successive droplet impingement has a great influence on the maximum spreading radius. For example, at $\Theta_E = 45^o$, the decrease of the maximum radius (R^*_{max}) between the advancing, and receding cases is approximately 20%, but for $\Theta_E = 120^o$ it is less than 5%. Figure 5.30 (c) shows the final radius of the droplet after it reaches equilibrium. For $\Theta_E = 120^o$, an extremely nonwettable condition, the final radius of wetting process is almost zero.

Hence, there are only five equilibrium angles listed on the plot legend. The plot shows only two trends of single and successive impingement. For the successive droplet impingement, the final radii of all three successive phases are the same. The trends of both single and successive impingements are a linear decrease, varying inversely with the equilibrium contact angle.

5.2.5 Successive droplet impingement with variation of fluid properties

The effects of property values of viscosity and surface tension on successive impingement are shown in Figure 5.31 using the nondimensional values μ^* and σ^*, respectively. Increasing viscosity reduces the radius, as might be expected, consistently for all successive impingement cases. The reduction seems to be insensitive to impingement phase condition. Shown in Figure 5.31 (b), there is a greater reduction of radius between the advancing and receding cases for the low surface tension case when compared to the high surface tension case. This seems to indicate that when the surface tension is high, the phase condition has little effect on total spreading. However, when the surface tension is low, the phase relationship is important, indicating that the viscosity has a more important effect on the total spreading extent when the surface tension is low.

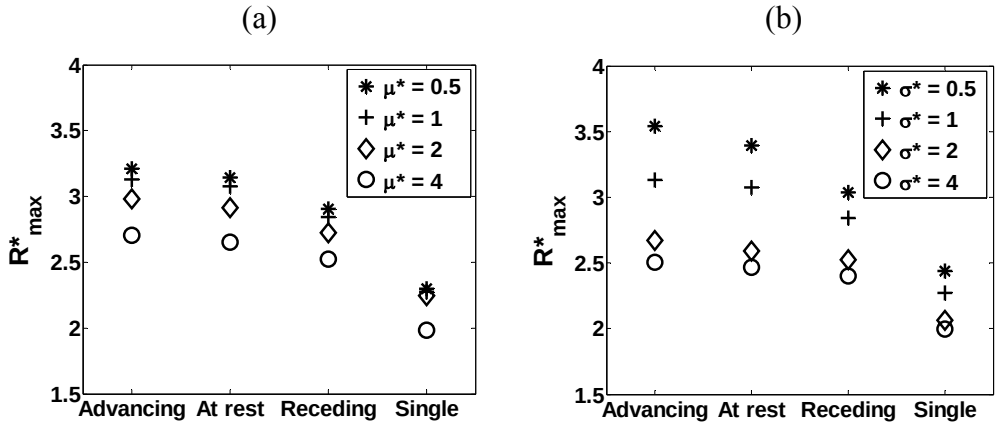

Fig. 5.31. Successive droplet spreading radius, R^*_{max} vs phases of the first impinging droplet subjected to successive impingement phase with $\Theta_E = 75^o$: (a) effect of viscosity, μ^*, and (b) effect of surface tension, σ^*.

CHAPTER 6

CONCLUSION

6.1 DROPLET FORMATION

Computational simulations are provided and used to investigate the droplet formation process with fluid structure interaction causing nozzle plate deflection. The effect of the piezoelectric waveform causes different characteristics of the droplet formation process. The step-function waveform ejects the droplet from the nozzle with a greater velocity than the pulse-function waveform. The required impulse needed to eject the droplet for a step function is determined to be $I^* = 0.3$. The drop volume does not change significantly with a decrease in I^*. For a flexible nozzle plate it is found that the major parameter that determines the characteristics of the droplet formation process is the pressure at the nozzle exit. Results show that it is possible to control the droplet volume and velocity by the characteristics of the vibrating nozzle plate. Surface tension is an important parameter dominating the droplet formation process. The combination of a large surface tension and very flexible nozzle plate can result in no droplet formation. The desired characteristics of the droplet formation (volume and momentum) can help determine the design of a flexible nozzle plate to deliver appropriate drops. For full understanding of a droplet generator design capabilities, a range of waveforms and generator geometries would need to be studied.

6.2 DROPLET IMPINGEMENT

Numerical simulations are presented which investigate single and successive droplet impingement with consideration of the effects of the dynamic contact angle, equilibrium contact angle, surface tension and viscosity. With the empirical-based molecular kinetic (M-K) theory, the dynamic contact angle during

the spreading and receding processes is determined. It is found that the equilibrium contact angle, in the droplet impinging process, affects not only the dynamic contact angle, but consequentially the spreading characteristics which include the damping ratio and maximum spreading radius. On the other hand, the equilibrium contact angle is shown to have a small effect on the contact line velocity. The higher level of wettability results in a significantly greater spreading radius and a smaller recoiling radius. This behavior is represented by the damping ratio (C_o). For wettable conditions ($\Theta_E < 90^o$), the spreading process has a higher damping ratio for the system with the lower equilibrium contact angle. Also, the successive droplet impingement shows that during the advancing phase of the first droplet, the impinging of the successive droplet causes the largest spreading radius compared to later phases: during receding, and at equilibrium. For nonwettable condition, the phases of successive droplet impingement do not greatly affect the maximum spreading radius, but they still generate greater spreading radii as compared to single droplet impingement. The viscosity and surface tension interaction is shown to affect successive droplet spreading. By impinging a successive droplet during the advancing phase of the initial droplet a complex recirculating flow pattern is found to exist which may enhance transport characteristics.

5.3 FUTURE REASEARCH WORK ON DROPLET FORMATION AND IMPINGEMENT

According to the results from this research, the numerical computation tools used show promising results to better understand the hydrodynamics of droplet formation and droplet impingement. Below are some fields of study suggested for future work.

1. Experimental and numerical studies of the pinch-off criteria are one important field of work to understand the behavior of the fluid filament at break-off. In this work, the pinch-off criteria is defined by the grid size and value of VOF variable. To gain more accurate results, the pinch-off model might be added to the numerical solver, and this may better match the physics at the pinch-off thread.
2. The effect of surface roughness on the droplet spreading and receding process would be an important research area. By applying the dynamic contact angle model along with the variation of the surface friction forces, the characteristics of droplet impingement could be studied. The friction force from wall roughness would be applied to the source term, F_i, determined by the viscous force and near-wall velocity.
3. The complete experimental study of the dynamic contact angle model is an important area to help find a proper model that could present the contact angle simply as a function of contact line velocity and the fluid properties and to validate the constants used from the curve fit of the M-K theory to other experimental results.
4. Splash droplet impingement is also a promising area that may be extended from this research. In the current work, the non-splash condition of droplet is assumed. To move this work into a splash condition, the un-axisymmetric impinging results would be required. The numerical model needs to use a 3D arbitrarily refined mesh in order to capture the fine detail of the splash impingement.

BIBLIOGRAPHY

1. Adams, R.L., and Roy, J., 1986, "A One-Dimensional Numerical Model of A Drop-on-Demand Ink Jet", Journal of Applied Mechanics, vol. 53, pp 193-197.
2. Amabili, M., 1994, "Modal properties of annular plates vibrating in water", The First International Conference on Vibration Measurements by Laser Techniques, Advances and Applications, Ancona, Italy.
3. Bayer, I.S. and Megaridis, C.M., 2006, "Contact angle dynamics in droplets impacting on flat surface with different wetting characteristics", J. Fluid Mech., vol. 558.
4. Beasley, J.D., 1977, "Model for Fluid Ejection and Refill of an Impulse Drive Jet," Journal of Applied Photograph.Engineering vol. 3.
5. Blake, T.D., 1993, "Dynamic contact angles and wetting kinetics", Wettability, Marcel Dekker.
6. Blake, T.D., and Haynes J. M., 1969, "Kinetics of liquid/liquid displacement", J. Coll. Interf. Sci., vol. 30.
7. Bourouina, T., and Grandchamp, J., 1996, "Modeling micropumps with electrical equivalent Networks," J. Micromech. Microeng., vol. 6.
8. Brackbill, J. U., Kothe, D. B., and Zemach, C., 1992, "A Continuum Method for Modeling Surface Tension," J. Comp. Phys., vol 100.
9. Bradley, S.G., and Stow, C.D., 1978, "Collisions between Liquid Drops", Phil. Trans. R. Soc. Lond. A. vol. 287.
10. Brenner, M. P., Eggers, J., Joseph, K., Nagel, S. R., and Shi, X. D., 1997, "Breakdown of scaling in droplet fission at high Reynolds numbers". Phys. Fluids, vol. 9.

11. Egger, J., 1993, “Universal Pinching of 3D Axisymetric Free-Sufface Flow”, Phys. Rev. Let., volume 71.
12. Eggers, J., 1995, “Theory of drop formation”, Physics of Fluids, vol 7.
13. Engel, O.G., 1955, “Water drop collisions with solid surfaces,” Journal of Research of the National Bureau of Standards, vol. 54.
14. Fawehinmi1, O.B., Gaskell, P.H., Jimack, P.K., Kapur1, N., and Thompson1, H.M., 2005, “A combined experimental and computational fluid dynamics anglysis of the dynamics of droplet formation”, J. Mech. Engr. Sci., vol. 219.
15. Ford, R. E., and Furmidge, C.G., 1967, “The formation of drops from viscous water-in-oil emulsions sprayed through fan-jet nozzles”, Br. J. Appl. Phys., vol 18.
16. Fromm, J.E., 1984, “Numerical Calculations of the Fluid Dynamics of Drop-on-Demand Jets,” IBM J. Res. Dev., vol. 28.
17. Glasstone, S., Laidler, K.J., and Eyring, H.J., 1941, “The Theory of Rate Process”, McGraw-Hill, New York.
18. Harlow, F.H., and Shannon, J.P., 1967, “The Splash of a Liquid. Droplet”, Journal of Applied Physics, vol 38.
19. Hartley, G.S., Brunskill, R.T., 1958, “Phenomena in Chemistry and Biology,” Pergamon Press, London.
20. Hawke, S., 2007, “Effects of a Thin, Flexible Nozzle on Droplet Formation and Impingement”, Master Degree Thesis, Oregon State University.
21. Henderson, D. M., Pritchard, W. G., and Smolka, L. B., 1997, “On the pinch-off of a pendant drop of viscous liquid., Phys. Fluids, vol. 11, 3188–3200.
22. Hermann, S., and Joachim, H., 2004,“Modelling of a microfluidic device with piezoelectric Actuators,” J. Micromech. Microeng., vol 14.

23. Hirt, C.W. and Nichols, B.D., 1981, “Volume of Fluid (VOF) Method for the Dynamics of Free Boundaries,” J. Comp. Phys., vol 39.
24. Hoffman, R.L., 1975, “A Study of the Advancing Interface”, J. Coll. Interf. Sci., vol. 50.
25. James, A.J.,Smith, M.K., and Glezer, A., 2003, “Vibration-induced drop atomization and the numerical simulation of low-frequency single-droplet ejection”, J. Fluid Mechanics, vol 476, pp. 29-62.
26. Krevet, B., and Kaboth, W., 1998, “Coupling of FEM programs for simulation of complex systems,” MSM98 (Santa Clara, CA).
27. Kubota, Y., and Suzuki, T., 1984, “Added mass effect on disk vibrating in fluid”, Transactions of the Japan Society of Mechanical Engineers, vol. 50.
28. Kyser, E.L., Collins, L.F., and Herbert, N., 1981, “Design of an Impulse Ink Jet”, Journal of Applied Photograph.Engineering vol. 3.
29. Leissa, W., 1969, “Vibrations of Plates”, NASA SP-160.
30. Liu, J., Franco, W., and Aguilar, G., 2005, “The effect of roughness on the impact dynamics and heat transfer of cryogen droplets impinging onto indented skin phantoms”, Proceeding of HT2005, 2005 ASME Summer Heat Transfer Conference, San Francisco, California, USA.
31. Lord Rayleigh, 1892, “On the Instability of a Cylinder of Viscous Liquid under Capillary Force,” Phil. Mag. 34.
32. Madejski, 1976, “Solidification of droplets on a cold surface”, International Journal of Heat and Mass transfer, vol. 19.
33. Minamikawa, T., Fujimoto, H., Hama, T., and Takuda, H., 2007, “Numerical Study of the Collision Dynamics and Heat Transfer of Water Droplets Impinging on a Hot Solid”, ISIJ International, vol. 47.

34. Percin, G., Lundgren, T.S., and Khuri-Yakub, B.T., 1998, “Controlled ink-jet printing and deposition of organic polymers and solid-particles,” in *Applied Physics Letters*, vol. 73.
35. Rao, J. S., 1999, “Dynamics of Plates”, Narosa Pub. House.
36. Rao, S.S., 1986, “Mechanical Vibration”, Addison-Wesley.
37. Renardy, M, 1994, “Some Comments on the surface tension driven break-up (or the lack of it) of viscoelastics jets”, J. Non-Newt. Fluid Mech. 51: 97–105 (1994).
38. Renardy, M., 1995, “A numerical study of the asymptotic evolution and breakup of Newtonian and viscoelastic jets”, Journal of Non-Newtonian Fluid Mechanics. Vol. 59.
39. Rioboo, R., Morengo, M., Tropea, C., 2002, “Time evolution of liquid droplet impact onto solid, dry surfaces,” Exp. Fluids, vol. 33.
40. Roisman, I.V., Rioboo, R. and Tropea, C.**,** 2002, “Normal impact of a liquid drop on a dry surface: model for spreading and receding”, Proc. R. Soc. Lond. A..
41. Shield, T. W., Bogy, D. B., and Talke, P. E., 1987, “Drop Formation by DoD Ink-jet Nozzles: A Comparison of Experiment and Numerical Simulation,” IBM J. Res. Dev., vol. 31.
42. Sikalo, S., Wilhelm, H.D., Roisman, I.V., Jakirlic, S., and Tropea, C., 2005, “Dynamic contact angle of spreading droplets: Experiments and simulations”, Physics of Fluids.
43. Stow, C.D., Hadfield, M.G., 1981, “An experimental investigation of fluid flow resulting from the impact of a water drop with an unyielding dry surface,” Proc. R. Soc. Lond. A: Math. Phys. Sci..

44. Tong, A.Y, Kasliwal, S., Fujimoto, H., and Takuda, T., 2004, "A numerical study on the successive impingement of droplet onto a substrate", Proceeding of ASME IMECE 2004, Anaheim, CA, IMECE2004-60813.
45. Trapaga, G., and Szekely, J., 1991, "Mathematical Modeling of the Isothermal. Impingement of Liquid Droplets in Spraying Processes", Metallurgy Trnasaction B, vol 2.
46. Ugural, A.C., 1981, "Stresses in Plates and Shells", McGraw-Hill.
47. Vadillo, D., Desie, G., and Soucemarianadin, A., 2004, "Spreading Behavior of Single and Multiple Drops," Laboratoire des Ecoulements Geophysiques et Industriels (LEGI), and AGFA-Gevaert Group N.V., XXI ICTAM, 15-21 August 2004, Warsaw, Poland.
48. Vogel, S.M., and Skinner, D.W., 1965, "Natural Frequencies of Transversely Vibrating Uniform Annular Plates", Journal of Applied Mechanics, vol. 32.
49. Von Karman, 1910, "Festigkeitsprobleme in Machinenbau", Encl. Der Math. Wiss.,vol. 4.
50. Weber, C., 1931, "Zum Zerfall eines Fliissigkeitsstrables," Z. Angew. Mafh. Mech. 11, pp 136.
51. Wijshof, H., 2004, "Free surface flow and acousto-elastic interaction in piezo inkjet," Nanotech vol. 2.
52. Worthington, A. M., 1876, "On the forms assumed by drops of liquid falling vertically on a Horizontal plate," Proc. R. Soc. London**,** vol 11.
53. Xu, H., Shirvanyants, D., Beers, K., Matyjaszewski, K., Rubinstein, M., and Sheiko1, S.S., 2004, " Molecular Motion in a Spreading Precursor Film", Phys. Rev. Lett., vol. 93.

54. Yang, A., and Tsai, W., 2006, “Ejection Process Simulation for a Piezoelectric Microdroplet Generator”, Tran. ASME, vol. 128.

55. Yang, G., and Liburdy, J. A., 2004, “Droplet Formation from a Pulsed Vibrating Micro-Nozzle”, Proceedings of the ASME Heat Transfer/Fluids Engineering Summer Conference 2004, pp 269-276.

56. Yarin, A.L., 1993, “Free Liquid Jets and Films: Hydrodynamics and Rheology,” Longman, Harlow.

57. Zhang, X., and Basaran, O.A., 1997, “Dynamic Surface Tension Efects in Impact of a Droplet with a Solid Surface”, Journal of Colloid and Interface Science, vol 187.